PAPER

Investigation of conventional and Super-X divertor configurations of MAST Upgrade using scrape-off layer plasma simulation

View the article online for updates and enhancements.

Related content

- SOLPS analysis of the MAST-U divertor with the effect of heating power and pumping on the access to detachment in the Super-x configuration
E Havlíková, J Harrison, B Lipschultz et al.

- Benchmarking of a 1D scrape-off layer code SOLF1D with SOLPS and its use in modelling long-legged divertors
E Havlíková, W Fundamenski, F Subba et al.

- Chapter 4: Power and particle control
A. Loarte, B. Lipschultz, A.S. Kukushkin et al.

Recent citations

- A review of radiative detachment studies in tokamak advanced magnetic divertor configurations
V A Soukhanovskii

- Overview of progress in European medium sized tokamaks towards an integrated plasma-edge/wall solution
H. Meyer *et al*

- Non-linear MHD simulations of ELMs in JET and quantitative comparisons to experiments
S Pamela *et al*

Investigation of conventional and Super-X divertor configurations of MAST Upgrade using scrape-off layer plasma simulation

E Havlíčková[1], W Fundamenski[2], M Wischmeier[3], G Fishpool[1] and A W Morris[1]

[1] EURATOM/CCFE Fusion Association, Culham Science Centre, Abingdon, Oxon, OX14 3DB, UK
[2] Imperial College of Science, Technology and Medicine, London, UK
[3] Max-Planck Institut für Plasmaphysik, EURATOM Association, Garching, Germany

E-mail: eva.havlickova@ccfe.ac.uk

Abstract

One of the first studies of MAST Upgrade divertor configurations with scrape-off layer plasma simulation (SOLPS) 5.0 are presented. We focus on understanding the main prospects associated with the novel geometry of the Super-X divertor (SXD). This includes a discussion of the effect of magnetic flux expansion and volumetric power losses on the reduction of target power loads, the effect of divertor geometry on the divertor closure and the distribution of neutral species and radiation in the divertor, and the role of the connection length in broadening the target wetted area. A comparison in conditions typical for MAST inter-ELM H-mode plasmas confirms the improved performance of the Super-X topology resulting in significantly better divertor closure with respect to neutrals (the atomic flux from the target increased by a factor of 6, but the atomic flux from the divertor to the upper SOL reduced by a factor of 2), increased radiation volume and increased total power loss (a factor of 2) and a reduction of target power loads through both magnetic flux expansion and larger volumetric power loss in the divertor (a factor of 5–10 in attached plasmas). The reduction of the target power load by SXD further increases with collisionality (high density or detached regimes) thanks to the larger importance of volumetric power losses. It is found that a cold divertor plasma leads to stronger parallel temperature gradients in the SOL which drive more parallel heat flux, meaning that the effectiveness of perpendicular transport in spreading the power at the target can be reduced, and this needs to be taken into account in any optimization.

Keywords: Super-X divertor, MAST, SOLPS, divertor design, transport codes

(Some figures may appear in colour only in the online journal)

1. Introduction

Advanced divertor geometries such as Snowflake or Super-X divertors (SXD) [1, 2] are presently investigated as alternative configurations for future reactors, with an effort to provide solutions for power exhaust issues. The major aim is to effectively reduce power loads to divertor targets which could, in large devices, exceed a tolerable maximum set by material limits. In this paper, we study the effects of the SXD which

will be installed on the MAST tokamak [3]. Another expected benefit of such a divertor is an improved closure, hence a higher neutral pressure in the divertor, but limited penetration of fuelling species neutrals and impurities into the region above the X-point.

2D scrape-off layer (SOL) transport codes such as scrape-off layer plasma simulation (SOLPS) [4] have proven to be helpful in quantifying the effects of geometry on the divertor performance and have been used to support the divertor design,
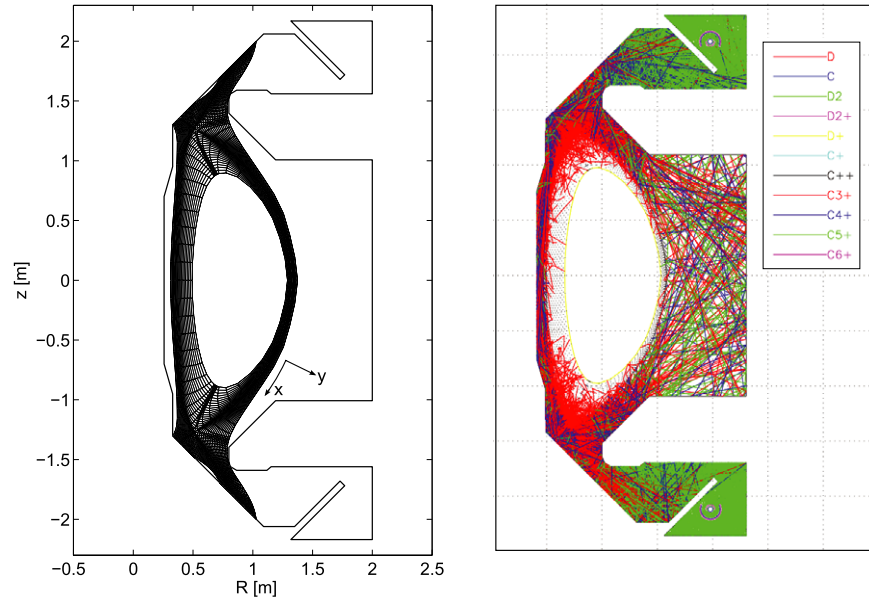
Figure 1. On the left, a SOLPS grid for the CD geometry (limited by the contact point with the baffle). Both Cartesian coordinates (R,z) and magnetic field coordinates—poloidal and radial (x,y)—are defined. On the right, the domain for the EIRENE simulation.

e.g. on ITER [5]. On the MAST tokamak, recent SOLPS5.0 simulations focused on optimization of the baffle positioning with respect to retaining the divertor closure, but avoiding a large flux on the baffle surfaces [6]. The effect of the Super-X divertor was preliminarily investigated also in [7, 8] by SOLPS5.0 and in [9] by a 1D code SOLF1D. Some of the latest results also concentrate on drift effects [10, 11].

Here we focus on the overall impact of the Super-X topology on the divertor performance in attached plasmas without impurity puffing. Simulations are based on two configurations proposed for MAST Upgrade (MAST-U): (i) a short-legged divertor (CD: the conventional divertor) which is closer to divertors in present machines (section 3), (ii) a long-legged divertor (SXD) with more complex magnetic topology employing additional poloidal coils in order to increase the connection length $L_\parallel$ and expand the plasma to a larger radius (section 4). The potential to optimize the effect of SXD in high density regimes and seeded plasmas will be discussed at the next stage.

Beside a direct comparison of the two configurations for inter-ELM H-mode plasmas, the sensitivity of the results to various factors has been studied. This includes scans for both physics parameters (such as input power to the SOL, density, radial transport coefficients, sputtering, gas puff location) and simulation parameters (e.g. fluid versus kinetic neutrals, heat flux limiters). As a baseline for MAST-U predictions, SOLPS5.0 results for MAST discharges, both L-mode and H-mode, are currently being validated against experiment as a separate work. With regards to the limits of the codes as SOLPS and common problems with the interpretation of experimental results, the paper focuses on a comparative study of CD and SXD, rather than trying to quantitatively reproduce a MAST experiment. The study presented here is extended in [12] from low density attached conditions to high density and detached regimes.

2. Simulation of the CD

2.1. Simulation setup

The divertor design for MAST-U offers large flexibility in terms of magnetic topology. One of the possible configurations is a CD shown in figure 1. SOLPS5.0 including EIRENE is used to study inter-ELM H-mode plasmas in this magnetic configuration with parameters typical for current MAST H-mode discharges. This section is to give a summary of the main results for the CD for the purpose of comparison with results for the Super-X magnetic configuration in the second part of the paper.

We define a case (a) with $P_{\rm inp} = 1.7$ MW (the total input power to the grid), $n_{\rm core} = 2.8 \times 10^{19}$ m^{-3} (the density at the inner boundary of the grid). The temperature and density drop across the pedestal is imposed by a transport barrier in perpendicular diffusivities (figure 2) which are otherwise poloidally uniform. These diffusivities are based on [11] and an earlier benchmarking of SOLPS with experiment [13].

As the SOL collisionality and the SOL width are important parameters of the SOL, we analyze three additional simulations defined in table 1: case (b) with larger radial transport assuming $D_\perp = 1$ m^{2}s^{-1} and $\chi_\perp = 1$ m^2 s^{-1} (shown in figure 2 as a dashed line), case (c) with double $n_{\rm core}$, case (d) with half $P_{\rm inp}$. While case (d) gives SOL temperatures comparable to those observed in the current MAST experiment, case (a) allows for a larger heating power available in MAST-U. Case (b) will be referred to as L-mode (here meaning wider SOL, noting that L-mode in MAST is usually a low power Ohmic plasma, below 1.7 MW).

Apart from deuterium plasma species, sputtered carbon impurities are taken into account, assuming both physical and chemical sputtering and the chemical sputtering yield of 1%. The effect of a larger sputtering of 3% will be explored as well. The particle source is from the core and the flux crossing
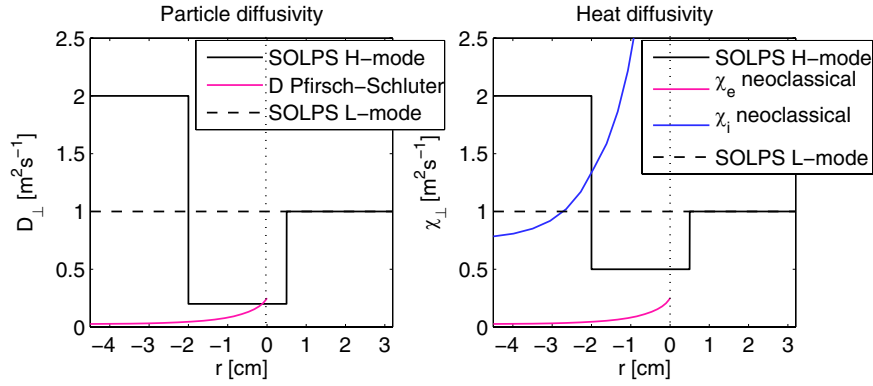
Figure 2. Radial diffusivities assumed in the code are compared with neoclassical Pfirsch–Schlüter values calculated from SOLPS profiles of the density and temperature for case (*a*) according to expressions given in [14]. The diffusion coefficients are plotted as functions of the radial coordinate at the midplane defined as $r \equiv R - R_{\mathrm{sep}}$ with the separatrix at $r = 0$.

Table 1. Definition of the four SOLPS simulations considered in the paper.

	(a)	(b)	(c)	(d)
n_{core} (10^{19} m^{-3})	2.8	2.8	5.6	2.8
P_{inp} (MW)	1.7	1.7	1.7	0.85
$D_{\perp}$ (m^2 s^{-1})	0.2	1.0	0.2	0.2
$\chi_{\perp}$ (m^2 s^{-1})	0.5	1.0	0.5	0.5

the separatrix is found to satisfy the given n_{core} mimicking particle fueling from a gas puff. The source is balanced by a flux on cryopumps which are located behind the outer targets (figure 1, right). The active pumping element of radius 2 cm gives a pumping speed of 42 m^3/s corresponding to a recycling coefficient $R = 0.9$ on this element (compared to 11 m^3/s in the current MAST experiment). Concerning parallel transport coefficients, the viscosity limiter $\beta = 0.5$ is used in all simulations following [15, 16]. The value of heat flux limiters is more questionable as it is more sensitive to the collisionality. Due to the lack of systematic study of kinetic corrections and their parametrization with plasma parameters, the heat flux here is prescribed by the classical Spitzer-Härm expression. Note that the simulation is toroidally symmetric and smooth targets (no imbrication) are assumed.

2.2. Plasma parameters

The first subjects of comparison between CD and SXD are the densities and temperatures in the divertor. Radial profiles of plasma parameters at the outer midplane and outer target are shown in figure 3 for cases (a) and (b) in CD. For given n_{core} and P_{inp}, the density and collisionality in the SOL is larger in case (b) as a result of larger $D_{\perp}$, while the temperatures at the midplane are lower in the near SOL, as well as in the divertor.

MAST Upgrade will have the capability to measure the $T_{\mathrm{i}}/T_{\mathrm{e}}$ ratio using the retarding field energy analyzer, see e.g. [17]. In the simulation, the temperature ratios of $T_{\mathrm{i}}/T_{\mathrm{e}} \approx 2$ are found at the midplane separatrix and go up to approximately 4 across the SOL. At the target, the temperature ratio ranges between 1 and 4 for the H-mode case (a), while we find approximately $T_{\mathrm{i}} \approx T_{\mathrm{e}}$ to $T_{\mathrm{i}} \approx 2T_{\mathrm{e}}$ for the L-mode case (b) as

the result of a stronger energy coupling between electrons and ions at higher collisionality.

By modifying the divertor geometry, one can achieve a broadening of the SOL (by effects of magnetic flux expansion and longer connection length), hence a reduction of the peak fluxes. The radial SOL width can be characterized by gradient lengths which are also shown in figure 3 and will be compared with SXD in section 3.2. The midplane gradient lengths from figure 3 ($\lambda_n = n_{\mathrm{e}}/|\nabla_r n_{\mathrm{e}}|$ and $\lambda_T = T_{\mathrm{e}}/|\nabla_r T_{\mathrm{e}}|$) range from $\lambda_n^{\mathrm{u}} \approx 1$ cm and $\lambda_T^{\mathrm{u}} \approx 0.5$ cm in the near SOL to $\lambda_n^{\mathrm{u}} \approx 2$–4 cm and $\lambda_T^{\mathrm{u}} \approx 2$–3 cm in the far SOL (index u as upstream). The SOL width in the upstream SOL and at the target (defining the target wetted area) and the peaking of target particle and energy fluxes are established as the result of competition between radial and parallel transport. Laminar transport codes as SOLPS are, however, unable to model radial transport self-consistently and therefore the gradient lengths in figure 3 are in principle given by the assumed radial transport coefficients.
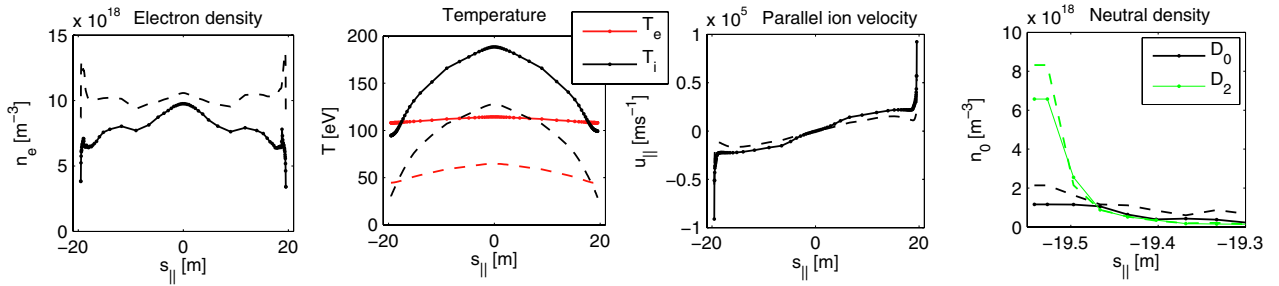
The parallel profiles in figure 4 (at the separatrix between the outer upper and lower targets) show sheath-limited SOL in the H-mode case (a) with flat T_{e} and low n_{e} at the target. With the peak target temperature of $T_{\mathrm{e}} \approx 100$ eV, the plasma is well attached and no pressure drop is observed along the field line (figure 3). In the L-mode case (b), the plasma temperature at the target is approximately $T_{\mathrm{e}} \approx 40$ eV, a small T_{e} gradient along the SOL is developed (smaller parallel heat conductivity $\kappa_{\mathrm{e}} \propto T_{\mathrm{e}}^{5/2}$, larger $\nabla_{\parallel} T_{\mathrm{e}}$) and stronger collisional cooling in the divertor (thanks to larger plasma and neutral densities and smaller temperatures) steepens $\nabla_{\parallel} T_{\mathrm{e,i}}$ further. The plasma remains attached at the given P_{inp}. The upstream collisionality is calculated in table 2, where the higher density and lower power cases (c) and (d) are included, all displaying low collisionality below 10, for which a sheath-limited SOL is expected and all with attached plasma with target temperatures above 20 eV. Note that the upstream and target parameters in table 2 for CD are similar to those found in simulations with the current MAST divertor.

2.3. Neutral species

The divertor closure with respect to neutral species or impurities is an important factor for the divertor performance.
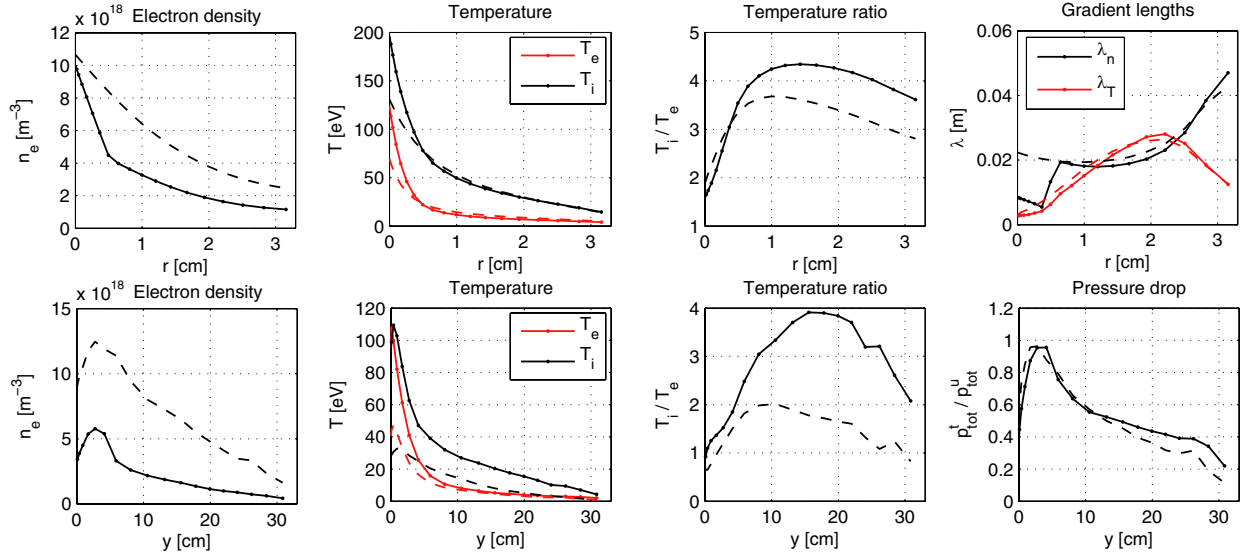
Figure 3. The CD configuration—(top) midplane radial profiles of (i) the electron density, (ii) the electron and ion temperature, (iii) the ratio of the temperatures, (iv) the gradient lengths of the density and temperature. (Bottom) target radial profiles of (i) the electron density, (ii) the electron and ion temperature, (iii) the ratio of the temperatures, (iv) the pressure drop along the SOL measured as the ratio of the target and upstream total pressure $p_{tot} = m_i n_e u_\parallel^2 + n_e k(T_e + T_i)$. Here y is the coordinate aligned with the target. Case (a) is shown as a solid line, while case (b) is shown as a dashed line.

Figure 4. The CD configuration—parallel profiles of (i) the electron density, (ii) the parallel ion velocity, (iii) the electron and ion temperature and (iv) the density of neutral species for cases (a) (solid) and (b) (dashed).

Table 2. The CD configuration—the collisionality of the SOL plasma ν_e and the mean free path λ_{ei} calculated as $\nu_e = L_\parallel / \lambda_{ei}$ and $\lambda_{ei} = 1.2 \times 10^{-4} (T_e^u)^2 / n_e^u [10^{20}]$ from the connection length $L_\parallel$, the upstream electron density n_e^u and the upstream electron temperature T_e^u in a flux tube just outside the separatrix. Target parameters are also shown (index t). The connection length $L_\parallel$ is defined as the parallel distance between the outer midplane and outer target.

|	$L_\parallel$ (m)	n_e^u (10^{19} m^{-3})	T_e^u (eV)	T_i^u (eV)	n_e^t (10^{19} m^{-3})	T_e^t (eV)	T_i^t (eV)	λ_{ei} (m)	ν_e
(a)	20	1.0	114	188	0.6	108	110	15.9	1.2
(b)	20	1.1	65	128	1.3	47	33	4.8	4.1
(c)	20	1.7	68	130	2.3	44	24	3.3	5.9
(d)	20	1.0	62	111	0.8	48	33	4.8	4.1

In the MAST-U design, a baffle structure has been introduced to separate the divertor region from the main plasma and to maintain neutral species below the X-point. The divertor closure is here evaluated by analyzing the distribution of neutrals and ionization sources. The 2D distribution of plasma species, neutrals and molecules in the divertor is displayed in figure 5 (for the meshed part of the vessel), illustrating regions where ionization and dissociation occur. In figure 6, the radial profiles of neutral species are shown for both H-mode and L-mode cases (a) and (b) at four different poloidal locations in the outer SOL. Molecules and neutrals are fairly

well separated from the main plasma as neutral densities at the baffle entrance are two orders of magnitude smaller than the densities in front of the target plate. Important will be the effect of the divertor geometry on the divertor closure discussed in section 3.3, where also the difference between the MAST-U divertor with a baffle and the current MAST configuration with an open divertor is addressed. In simulations of the open MAST divertor, one typically finds similar neutral densities at the target as in figure 6 (more neutrals escaping to the upper chamber, but less pumped into the divertor), but larger neutral densities at the midplane and in the core.
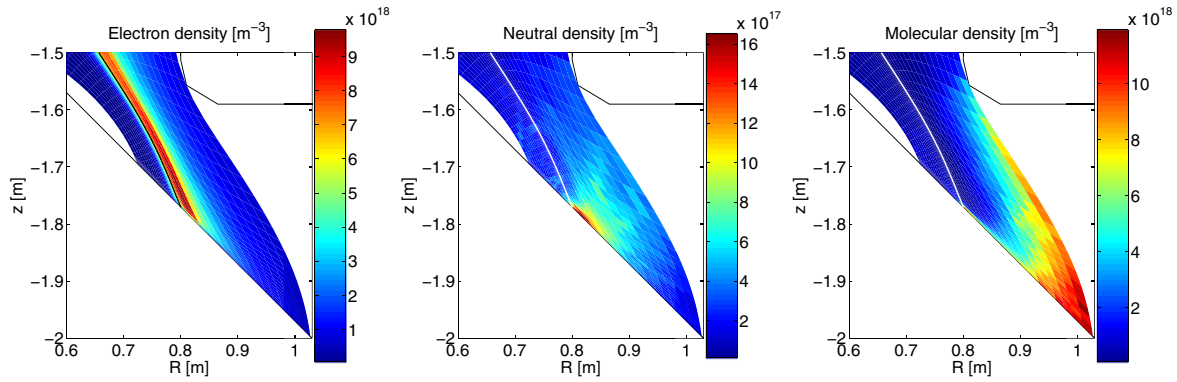
Figure 5. The CD configuration—distribution of electrons, D_0 and D_2 in the divertor leg in case (a).
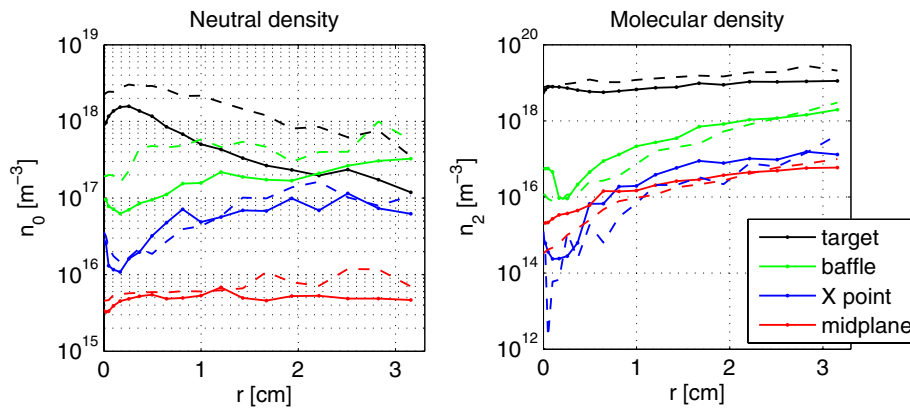
Figure 6. The CD configuration—radial profiles (mapped to the midplane to have a common scale) of the D_0 and D_2 density for case (a) (solid) and case (b) (dashed) at four poloidal locations in the outer SOL—at the target (black), at the contact point of the plasma grid with the baffle (green), at the X-point (blue), at the midplane (red).

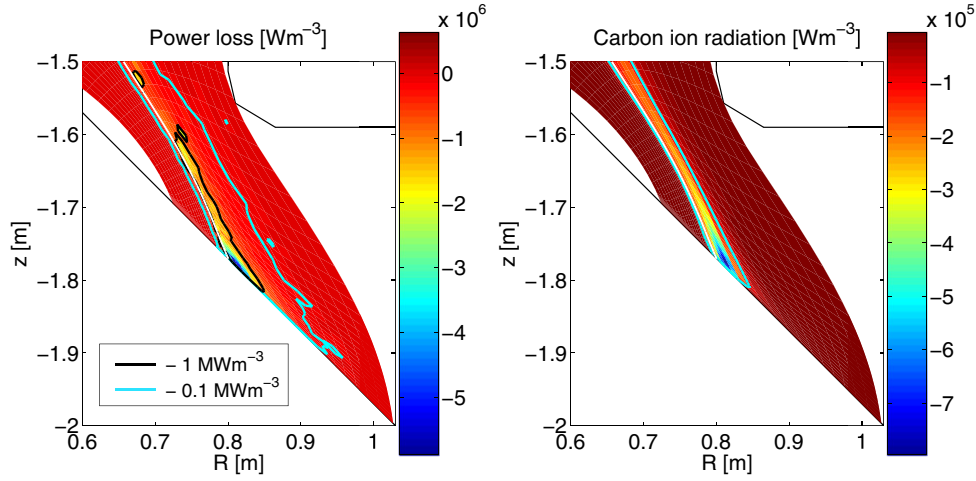## 2.4. Power losses and radiation

As the divertor geometry influences the collisionality and the divertor closure with respect to neutrals and impurities, it also affects radiation losses. One seeks solutions to increase the radiated power fractions as a mechanism to remove power from the plasma in the divertor volume before it is deposited at the target in a localized way. In that context, the effect of the divertor geometry is investigated by analyzing the distribution of power losses in the divertor and the sensitivity of radiation to parameters such as the connection length.

The volumetric power loss in the divertor leg of MAST-U is shown on the left of figure 7 for case (a), calculated as the total energy loss caused to the plasma due to impurity radiation and all plasma–neutral collisions including neutral radiation, charge-exchange and ionization processes (which are impossible to separate in the current version of SOLPS). The total power loss is strongest in a small region around the strike point (see the black contour line that defines a region where the energy loss is larger than $1\,\mathrm{MW\,m^{-3}}$), but a non-negligible power loss occurs in the divertor leg all the way up to the X-point (see the blue contour line that defines a region where the energy loss is larger than $0.1\,\mathrm{MW\,m^{-3}}$). 90% of the power loss in the divertor region displayed in figure 7 takes place in the region defined by the blue contour. This region extends into the half SOL radially and up to the X-point

poloidally and spreads over approximately 30% of the meshed divertor volume. The temperature range is this region changes from one case to another, depending on other parameters such as electron and neutral densities. In figure 7 on the right, carbon ion line radiation is shown separately, again extending up to the X-point.

For the L-mode case (b), the power loss region broadens radially up to 58% of the meshed divertor volume. This is indicated in figure 8 on the left, where the power loss in the SOL is plotted for each flux tube separately as a function of the target coordinate. Cases (c) and (d) with increased density and reduced input power are shown as well. In the higher density case, due to increased collisionality, the power loss region broadens and the total power loss increases similarly to case (b). figure 8 on the right separates carbon radiation and indicates that deuterium-based processes account for most of the power removal in the simulations at the given carbon sputtering yield.

Quantitatively, the power losses are presented in table 3 separately for the core, the SOL and the outer divertors. Table 3 shows that a large fraction of the power is lost in the region defined by the blue contour line in figure 7. The total volumetric power loss clearly grows in the L-mode case (b) and the higher density case (c). This is consistent with the increased surface/volume from which the power loss occurs.

Figure 7. The CD configuration—(left) distribution of total power losses in the divertor for case (a). The contour lines show regions in the divertor where the power loss exceeds a certain limit. (Right) distribution of carbon line radiation in the divertor.
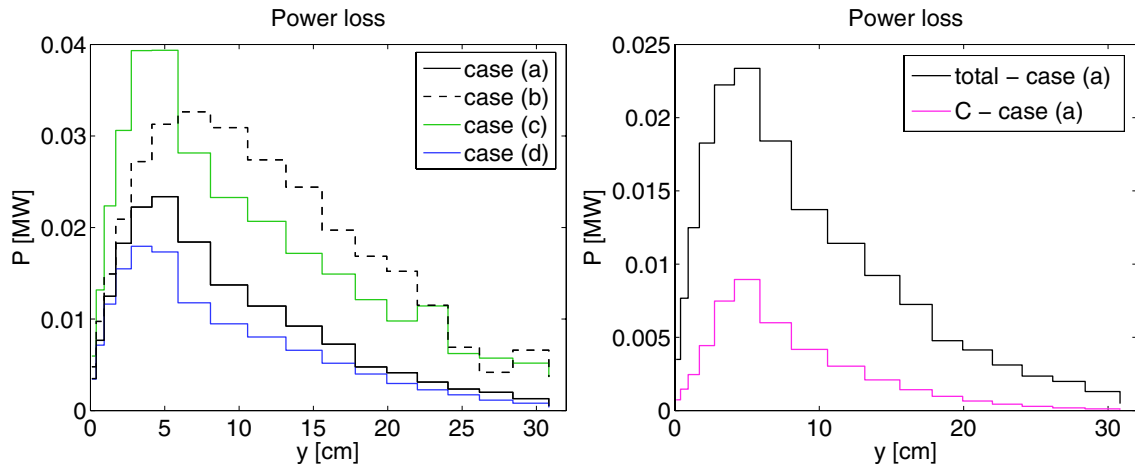

Figure 8. The CD configuration—(left) volumetric power losses in the outer SOL calculated for each flux tube individually. y is the target coordinate with 0 corresponding to the separatrix location. All four cases are shown—the H-mode case (a) (solid), the L-mode case (b) (dashed), the higher density case (c) (green) and the lower power case (d) (blue). (Right) the total power loss and the loss due to carbon radiation are shown for case (a).

Table 3. The CD configuration—the first four rows show the total volumetric power loss P_{vol} in terms of P_{inp} and the power loss due to carbon radiation separately in four SOLPS simulations (a), (b), (c) and (d) in different regions: (i) in the core (the closed field line part of the grid), (ii) in the SOL (the whole grid outside the separatrix), (iii) in the outer divertors (the region displayed in figure 7), (iv) in the blue region (defined in figure 7 by the contour line). The bottom rows show the surface S and the volume V of this region. The total power loss is calculated from EIRENE as the total energy loss caused to the plasma due to all plasma–neutral interactions including neutral and impurity radiation, charge exchange and ionization.

	Total				Carbon			
	(a)	(b)	(c)	(d)	(a)	(b)	(c)	(d)
P_{vol} in the core	4.4%	4.4%	2.6%	4.0%	1.1%	1.9%	1.6%	1.7%
P_{vol} in the SOL	11.5%	21.7%	21.6%	18.2%	3.6%	7.1%	7.1%	5.5%
P_{vol} in the outer divertors	7.4%	15.3%	14.5%	11.2%	1.2%	3.3%	3.6%	2.2%
P_{vol} in the blue region	6.7%	14.9%	13.9%	9.8%	0.9%	2.8%	3.1%	1.7%
S of the blue region [m^2]	0.043	0.081	0.066	0.037	0.016	0.031	0.021	0.013
V of the blue region [m^3]	0.209	0.403	0.329	0.177	0.076	0.145	0.099	0.059

To evaluate the effect of impurity radiation in the two different geometries, table 3 separates the power loss caused by carbon ion line radiation. In CD, the power fraction radiated by carbon reaches 9% in total (unseeded plasma with the chemical sputtering yield of 1% for carbon), and will be compared with SXD in section 3.4. The effect of carbon concentration has also been tested by increasing the sputtering coefficient to 3%. In CD, the power radiated by carbon in the SOL almost doubles from 4–7% to 6–13% and increases slightly in the core.
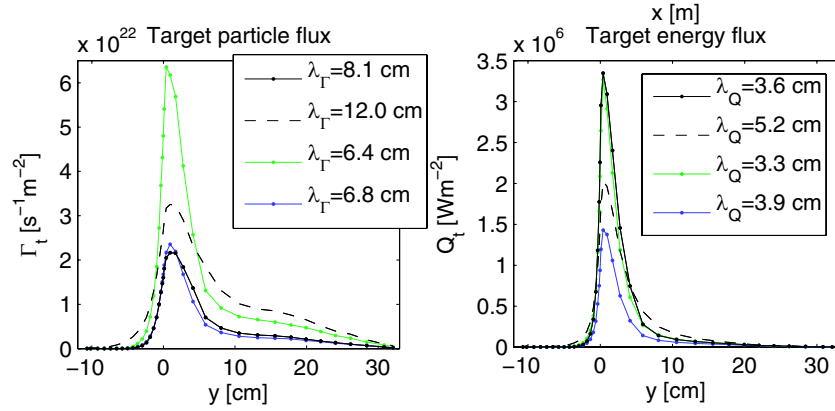
Figure 9. The CD configuration—particle (deuterium ions) and power (deuterium ions plus electrons) loads at the outer target as functions of the target coordinate *y* for case (a) (solid), case (b) (dashed), case (c) (green) and case (d) (blue).

2.5. Particle and energy fluxes

2.5.1. Target fluxes.
Particle and power loads to the outer target are shown in figure 9 for all four simulations. The target wetted area is characterized by the profile width at the target defined as

$$\lambda_\Gamma^t = \frac{\int \Gamma_t \mathrm{d}y}{\Gamma_t^{\max}}, \qquad \lambda_Q^t = \frac{\int Q_t \mathrm{d}y}{Q_t^{\max}}. \qquad (1)$$

$\lambda_\Gamma^t \approx 8.1$ cm and $\lambda_Q^t \approx 3.6$ cm are found for the case (a) (index t as target) and a factor of 1.5 larger for case (b). Mapped to the midplane as $\lambda^u = \lambda^t/\langle \mathrm{d}y/\mathrm{d}r\rangle$, the power decay length in the H-mode case (a) is $\lambda_Q^u \approx 0.3$ cm and the particle flux width is $\lambda_\Gamma^u \approx 0.6$ cm. To calculate the flux expansion factor $\langle \mathrm{d}y/\mathrm{d}r\rangle$, averaging over $\lambda_Q^t \approx 4$ cm is used for the energy flux and averaging over $\lambda_\Gamma^t \approx 8$ cm is used for the particle flux.

The profile width broadens in case (b) for both particles and energy due to increased radial diffusivities, consistently with reduced peak power load Q_t. The higher density case (c) has no effect on the power load (in attached conditions), while it causes a larger particle load Γ_t. For a two times lower input power in case (d), Q_t is reduced by a factor of 2, while Γ_t remains the same.

2.5.2. Flux expansion.
In novel divertor configurations such as SXD, an expansion of the plasma in the divertor region by magnetic geometry is used as one of the mechanisms to reduce the target energy flux. The effective flux expansion $\langle FX\rangle$ between the midplane and target locations for the CD case is shown in table 4 and will be compared with SXD in section 3.5.2. The total flux expansion of 6.0 is separated into the toroidal flux expansion $\langle FX_{\mathrm{tor}}\rangle$ of 0.6 (the outer strike point at smaller R than the outer midplane SOL), the poloidal flux expansion $\langle FX_{\mathrm{pol}}\rangle$ of 3.4 and the broadening caused by the target tilting $\langle FX_{\mathrm{tilt}}\rangle$ of 2.9 (defined in the appendix). The flux expansion factors are calculated using averaging over 4 cm which corresponds to λ_Q^t in the H-mode case (a) and they change only little for averaging over 8 cm (corresponding to λ_Γ^t) which is also shown in table 4.

Compared to the current MAST configuration with a horizontal target where the effective flux expansion is $\langle FX\rangle \approx$

Table 4. The CD configuration—flux expansion factors between the outer midplane and outer target.

	$\langle FX\rangle$	$\langle FX_{\mathrm{tor}}\rangle$	$\langle FX_{\mathrm{pol}}\rangle$	$\langle FX_{\mathrm{tilt}}\rangle$	$\langle \mathrm{d}y/\mathrm{d}r\rangle$
Average over λ_Q	6.02	0.61	3.40	2.89	11.61
Average over λ_Γ	6.68	0.62	3.39	3.16	12.84

2.3, the major change is in $\langle FX_{\mathrm{tilt}}\rangle$ which increases from approximately 1 to 3, while $\langle FX_{\mathrm{tor}}\rangle$ and $\langle FX_{\mathrm{pol}}\rangle$ do not change much. Thanks to the target tilting in CD, the peak Γ_t and Q_t are reduced compared to the current MAST divertor for the same total particle flux and power arriving at the target.

2.5.3. Global balance.
Global power balance and particle fluxes are calculated in table 5. Most of the power and particles cross the separatrix at the outer side (note that poloidally uniform $D_\perp$ and $\chi_\perp$ are assumed for simplicity in the model) and are therefore deposited mainly at the outer targets (connected double null). In the H-mode case (a) with low $D_\perp$ and $\chi_\perp$ and a narrow SOL, 76% of P_{inp} is deposited at the outer targets. In the cases (b, c, d), it is less than 70%, while more power goes to the outer wall or is radiated in the SOL. In all cases, the outer targets receive most of the power (60–80%) and the energy fluxes to the wall are only 1–2% of P_{inp}. The power balance is similar in simulations of the current MAST divertor in terms of the power deposited at the targets and the total power loss, with the difference that there is more power radiated in the core and less in the SOL in MAST with an open divertor compared to MAST-U with CD.

The applied version of SOLPS does not enable to separate the total power loss into individual components caused by different collision processes. Separately, impurity radiation and bremsstrahlung can be calculated. Changes have been made to the code to separate also neutral radiation and results are presented in [12]. Apart from radiation, it is assumed that the dominant power loss processes are charge exchange and ionization. Bremsstrahlung is negligible in MAST (0.1% here). The power fraction radiated by carbon is 5–9% of P_{inp} (accounts for approximately 30–40% of the total power loss) and increases by a factor of 2 with increased sputtering yield (3%) to 8–16% (corresponding to 40–45% of the total

Table 5. The CD configuration—the upper part of the table shows the power balance in the simulations. Expressed in % of $P_{\rm inp}$, the table shows: $P_{\rm sol,in}$ and $P_{\rm sol,out}$—the power crossing the separatrix on the inner or outer side, $P_{\rm t,in}$ and $P_{\rm t,out}$—the power deposited at the inner and outer targets, $P_{\rm wall}$—the power deposited at the outer boundary of the SOLPS domain (both inboard and outboard wall), $P_{\rm pfr}$—the power crossing the private flux region boundaries, $P_{\rm vol}$—the volumetric power loss, $P_{\rm vis}$—the viscous heating. It holds $P_{\rm inp} = P_{\rm vol} + P_{\rm t,in} + P_{\rm t,out} + P_{\rm wall} + P_{\rm pfr} - P_{\rm vis}$. The lower part of the table shows the particle flux crossing the separatrix $F_{\rm sol}$ from which $F_{\rm sol,out}$ crosses the separatrix at the outer side. $F_{\rm t,out}$ is the flux deposited at the outer targets and $F_{\rm wall,out}$ is the flux deposited at the outer wall expressed in terms of $F_{\rm t,out}$. All fluxes are calculated as sums over all ion species. Note that here the volumetric power loss $P_{\rm vol}$ is calculated from the balance between the input power and the fluxes deposited at the solid surfaces, see the equality above. This calculation of $P_{\rm vol}$ leads to a similar result as in table 3, proving the energy balance in the simulation is satisfied.

	(a)	(b)	(c)	(d)
$P_{\rm sol,in}$, $P_{\rm sol,out}$	11.9%, 82.7%	12.4%, 83.4%	12.8%, 84.0%	12.3%, 82.6%
$P_{\rm t,in}$, $P_{\rm t,out}$	13.3%, 75.9%	12.0%, 65.3%	12.0%, 67.9%	11.8%, 68.7%
$P_{\rm wall}$, $P_{\rm pfr}$	1.1%, 0%	2.2%, 0%	2.0%, 0%	1.8%, 0%
$P_{\rm vol}$	16.4%	24.2%	22.1%	23.0%
$P_{\rm vis}$	6.7%	3.7%	4.0%	5.3%
$F_{\rm sol}$	4.3×10^{21} s^{-1}	8.4×10^{21} s^{-1}	7.9×10^{21} s^{-1}	4.4×10^{21} s^{-1}
$F_{\rm sol,out}$	81.0%	84.9%	82.3%	81.4%
$F_{\rm t,out}$	2.0×10^{22} s^{-1}	4.3×10^{22} s^{-1}	4.4×10^{22} s^{-1}	1.8×10^{22} s^{-1}
$F_{\rm wall,out}$	1.9%	2.6%	2.0%	2.1%

power loss). This increases the total power losses and reduces the power to the outer targets. The combined effect of the sputtering yield and SXD will be discussed in section 3.5.4.

In all simulations, the divertor baffle receives only a small fraction of the particle flux with respect to the flux deposited at the target and therefore most of the recycling and sputtering takes place in the divertor. On the other hand, the divertor remains closed to neutrals thanks to the closed design with a baffle (see later in table 7).

3. CD versus SXD performance

3.1. Super-X geometry

One of the main design features of the new divertor in MAST-U are the additional poloidal coils in the divertor region (see e.g. [7]) that allow to vary the connection length in the divertor, the strike point location along the target and the expansion of the plasma in the divertor. This enables the Super-X magnetic geometry. One of the considered connected double null configurations is shown in figure 10. The double null topology benefits from the separation of the inner and outer SOL—most of the power goes to the outer side, where the divertor is modified to distribute the power over a larger target area. In figure 10, the magnetic configuration on the inner side does not change and in the simulation only a small change is found in plasma parameters on the inner side, therefore we focus mainly on results in the outer SOL.

The increased target wetted area in SXD is achieved by magnetic flux expansion, see section 3.5.2 and the appendix, which is a combination of poloidal flux expansion (reduced poloidal magnetic field in the vicinity of poloidal coils) and toroidal flux expansion (reduced toroidal magnetic field at larger radius). The corresponding drop of the total magnetic field B and its poloidal component B_x is shown in figure 10 for a flux tube in the near outer SOL.

Apart from the reduction of $Q_{\rm t}$ through magnetic geometry, larger volumetric power losses in SXD are expected due to higher collisionality and better divertor closure (higher neutral pressure in the divertor and reduced temperatures, i.e. stronger radiation rate), see sections 3.3 and 3.4.

The connection length increases from 20 to 35 m in a flux tube just outside the separatrix (at $r \approx 0.1$ mm), giving an opportunity for more power to be removed along the field line. The major increase occurs around the X-points and in the extended divertor region where the poloidal magnetic field is weak. It is expected that longer $L_\parallel$ leads to a broadening of the power deposition profile, hence a reduction of the peak load, as particles and energy have longer distance to travel before reaching the target, while they traverse radially (experimentally observed in [18]). This effect will be discussed in section 3.5.3.

3.2. Plasma parameters

Four SOLPS simulations with parameters listed in table 1 are repeated for the SXD configuration and compared with those in section 2 for CD. The same radial transport coefficients are used (see figure 2), as we do not yet have a basis for a different radial transport. We will see that such assumption gives similar conditions in the core and upstream SOL and this will represent the starting point of our comparison. At the same time, this approach gives an opportunity to separate changes in the divertor region from discrepancies in the upstream SOL.

Radial profiles of plasma parameters for the H-mode and L-mode cases (a) and (b) are shown in figure 11. While the midplane densities and temperatures are comparable to those in figure 3 for CD, a strong reduction of the temperatures in the divertor occurs in SXD as the result of collisional cooling and flux expansion, accompanied by an increase of the target density. The temperature ratio at the outboard midplane of SXD goes up to $T_{\rm i}/T_{\rm e} \approx 4$ (similar to CD), while it is reduced at the target compared to the CD case (stronger thermal coupling at larger n and smaller T as the result of the energy exchange between electrons and ions described by $Q_{\rm ei} \propto n^2 (T_{\rm e} - T_{\rm i})/T_{\rm e}^{3/2}$). The SOL width at the outboard midplane is comparable between CD and SXD for the same radial transport coefficients as shown by the radial
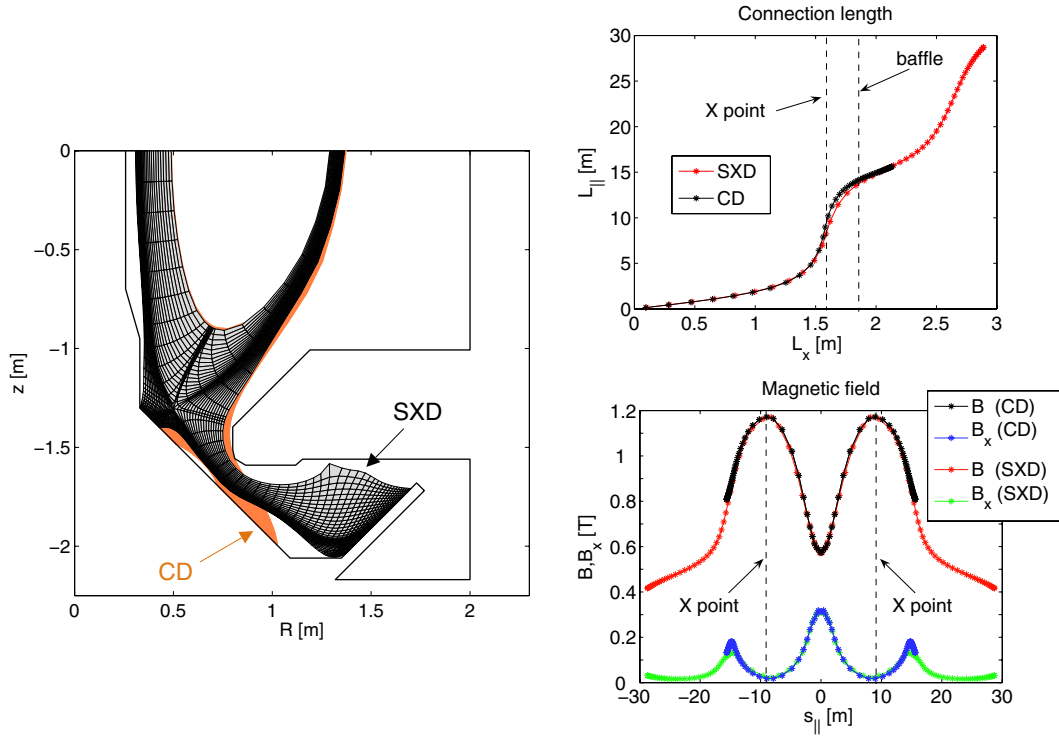
Figure 10. On the left, a SOLPS grid for the SXD geometry compared with the CD geometry. On the right, (top) the connection length $L_{\parallel}$ as a function of the poloidal distance from the outer midplane to the outer target L_x, (bottom) the total magnetic field B and the poloidal magnetic field B_x compared in the two configurations. B and $L_{\parallel}$ are shown on a flux tube in the near SOL which is defined as the flux tube with maximum power load at the target.
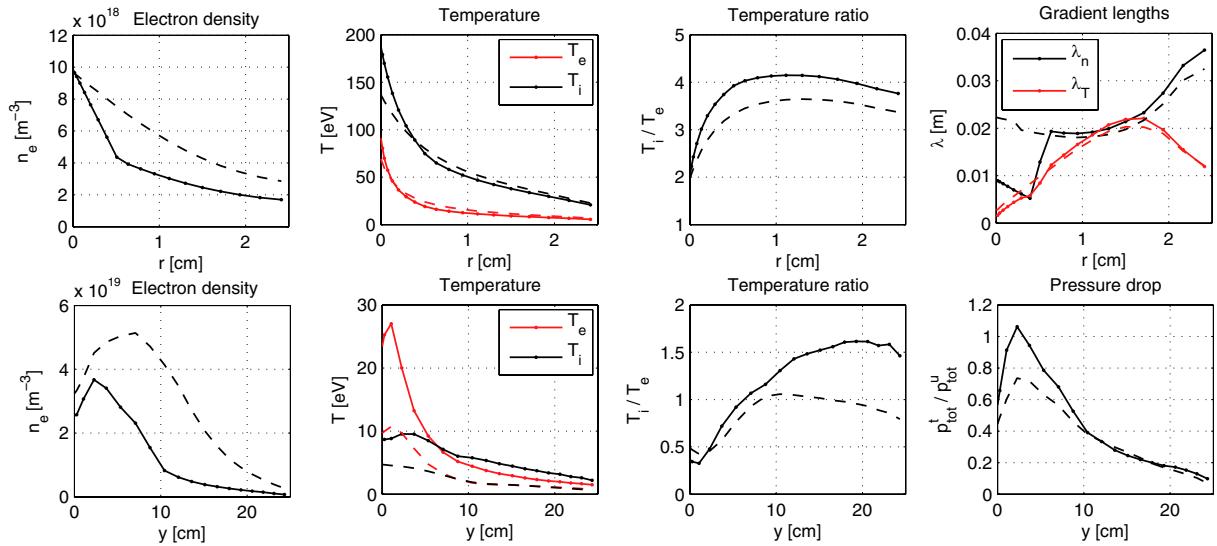
Figure 11. The SXD configuration—(top) midplane radial profiles of (i) the electron density, (ii) the electron and ion temperature, (iii) the ratio of the temperatures, (iv) the gradient lengths of the density and temperature. (Bottom) target radial profiles of (i) the electron density, (ii) the electron and ion temperature, (iii) the ratio of the temperatures, (iv) the pressure drop along the SOL measured as the ratio of the target and upstream total pressure $p_{\text{tot}} = m_i n_e u_{\parallel}^2 + n_e k(T_e + T_i)$. The SXD case (a) is shown as a solid line, while case (b) is shown as a dashed line. Compare with figure 3.

decay lengths in figures 3 and 11, and also later by a direct comparison of the outer midplane profiles in figure 13. In case (a) with reduced radial transport, the plasma is attached, while in case (b), a pressure drop along the field lines starts to form due to momentum losses as we approach lower target temperatures of $T_e \approx 10$ eV. Table 6 gives a summary of plasma

parameters in SXD in all four simulations, which range from attached plasma in case (a) to cases where the outer leg is not far from the detachment limit of $T_e \approx 5$ eV (b), (c), (d).
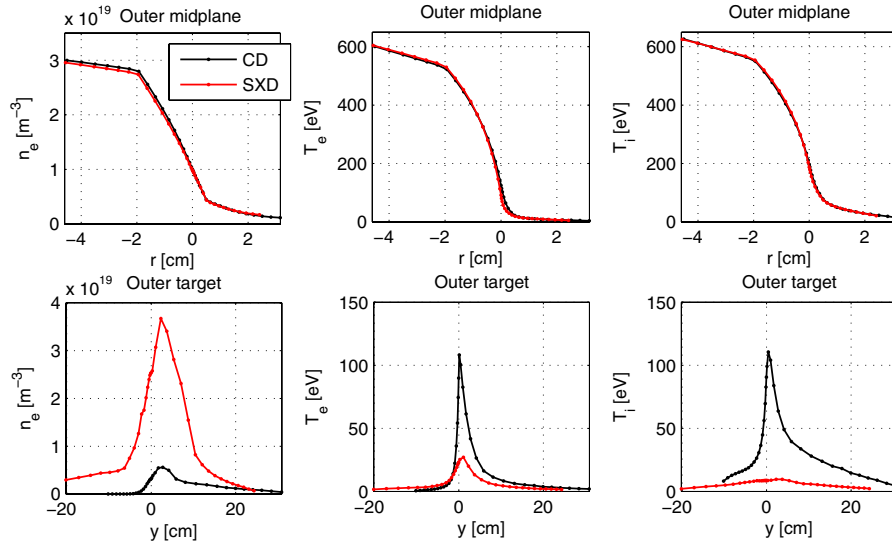
A direct comparison of the radial profiles for case (a) is presented in figures 12 (inner SOL) and 13 (outer SOL). Plasma parameters are strongly modified in the extended outer divertor

Table 6. The SXD configuration—the collisionality of the SOL plasma ν_e and the mean free path λ_{ei} calculated as $\nu_e = L_{\parallel}/\lambda_{ei}$ and $\lambda_{ei} = 1.2 \times 10^{-4}(T_e^u)^2/n_e^u[10^{20}]$ from the connection length $L_{\parallel}$, the upstream electron density n_e^u and the upstream electron temperature T_e^u in a flux tube just outside the separatrix. Target parameters are also shown (index t). Compare with table 2.

	$L_{\parallel}$ (m)	n_e^u (10^{19} m^{-3})	T_e^u (eV)	T_i^u (eV)	n_e^t (10^{19} m^{-3})	T_e^t (eV)	T_i^t (eV)	λ_{ei} (m)	ν_e
(a)	35	1.0	81	179	3.7	27.0	9.5	8.1	4.4
(b)	35	1.0	65	134	5.1	10.7	5.0	5.2	6.8
(c)	35	1.5	71	138	8.9	13.5	6.3	3.9	9.0
(d)	35	0.9	58	118	4.0	6.8	4.3	4.5	7.8
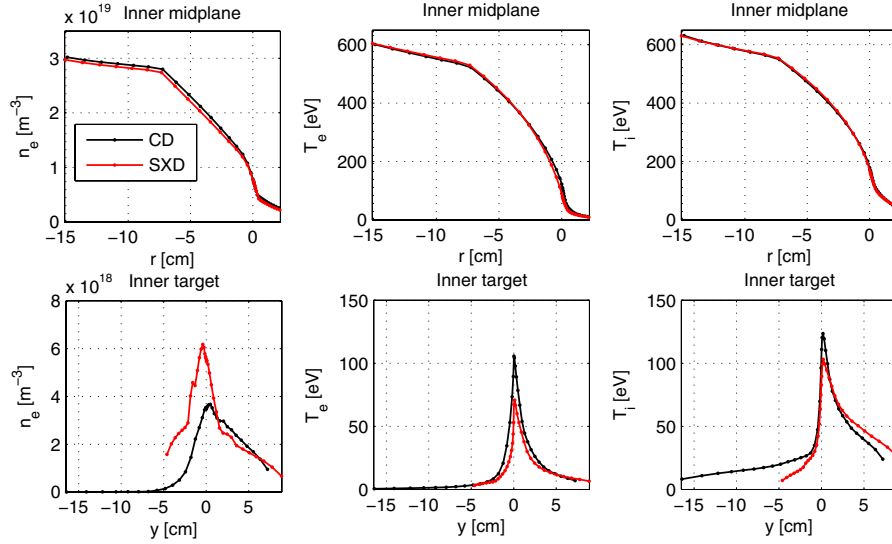
Figure 12. Direct comparison of radial profiles between CD (black) and SXD (red) for case (a) in the inner SOL.
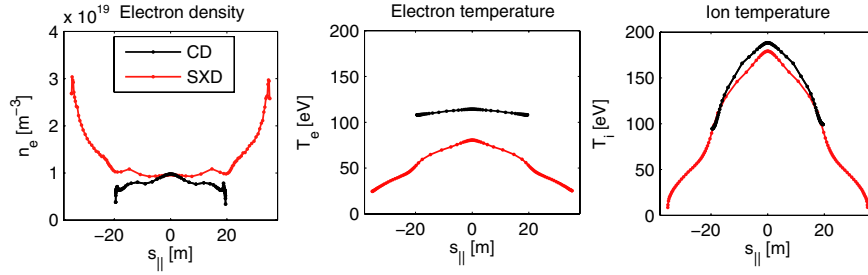

Figure 13. Direct comparison of radial profiles between CD (black) and SXD (red) for case (a) in the outer SOL.

which stays isolated from the rest of the plasma where the densities and temperatures remain rather unchanged. A small change in the inner divertor is caused by larger particle flux from the outer divertor across the private flux region resulting from the larger density in the outer leg in SXD.

Parallel profiles for case (a) are shown in figure 14. The modification of the divertor leads to a transition of the SOL from the sheath-limited regime with flat n_e and T_e into the high-recycling regime. The temperatures in the divertor drop as the result of stronger collisional cooling and flux expansion giving rise to steeper $\nabla_{\parallel}T$. This is accompanied by an increase in the density (constant total pressure along the field line) and stronger ionization source in front of the divertor plate. For the same pedestal density and input power into the SOL, the upstream n_e and T_i are unchanged, while the upstream T_e drops by several % as T_e tends to flatten out more than T_i due to

Figure 14. Direct comparison of parallel profiles between CD (black) and SXD (red) for case (a).
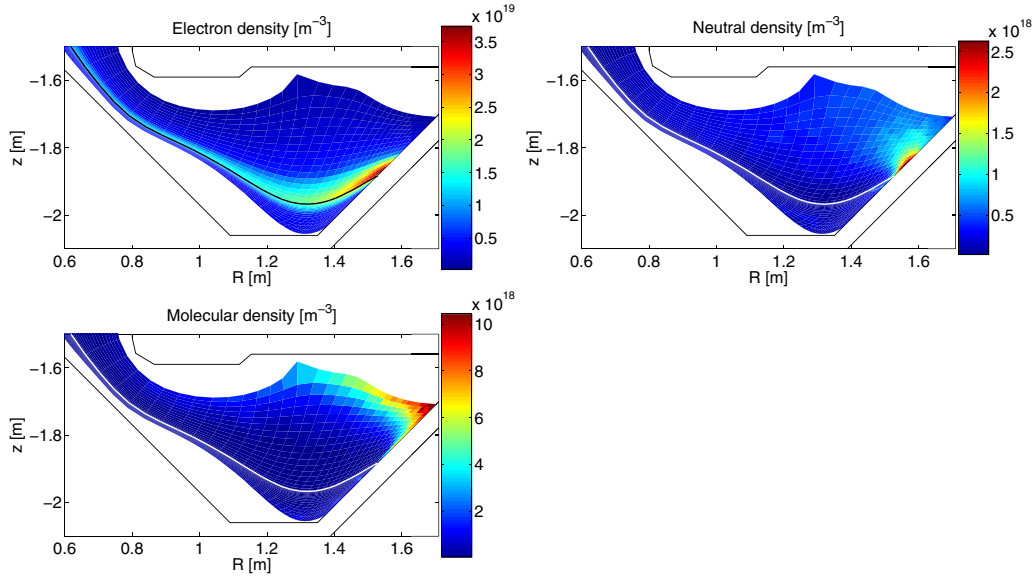
Figure 15. The SXD configuration—distribution of electrons, D_0 and D_2 in the divertor leg in case (a). Compare with figure 5.
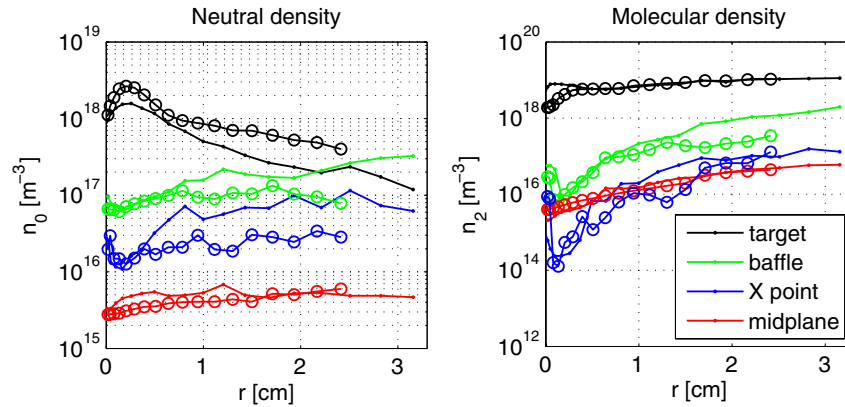
Figure 16. Radial profiles (mapped to the midplane) of the D_0 and D_2 density for case (a) in CD (points) and SXD (open circles) at four poloidal locations in the outer SOL—at the target (black), at the contact point of the plasma grid with the baffle (green), at the X-point (blue), at the midplane (red).

larger parallel conductivity (subject to heat flux limiters). In cases (b), (c), (d), all the upstream parameters n_e^u, T_e^u and T_i^u are comparable, see tables 2 and 6, and the reduction of the temperatures comes essentially from the divertor.

3.3. Neutral species

Due to larger plasma densities in the divertor in SXD, more neutrals are recycled at the target and larger neutral densities are found in SXD (figure 15) in comparison to CD (figure 5). Neutrals species stay better separated from the main plasma compared to figure 5 where D_0 and D_2 particles reach further towards the X-point. Radial profiles of the D_0 and D_2 densities are shown in figure 16 where the CD (points) and SXD (circles) H-mode cases are compared. The D_0 densities are increased at the target compared to CD, while they are reduced at the location of the baffle nose, the X-point and at the midplane. The molecular densities in both configurations are

Table 7. Fluxes of D_0 and D_2 in $[10^{21} \, s^{-1}]$ for three divertor configurations—MAST (before upgrade, see the geometry on the right), CD and SXD (MAST-U). The fluxes are integrated across specific surfaces defined in the plot on the right, poloidal fluxes (target, X-point) are calculated in the direction of the *x* coordinate and radial fluxes (core, PFR, main and divertor chambers) in the direction of the *y* coordinate.

	Atoms			Molecules			
	MAST	CD	SXD	MAST	CD	SXD	
Target	−2.77	−1.58	−10.34	−2.11	−3.35	−6.06	
X-point	−0.65	−0.90	−0.41	−0.22	−0.12	−0.01	
PFR	−0.24	−0.42	0.05	0.29	0.33	0.41	
Div. chamber	4.37	9.67	16.54	−0.47	−4.34	−7.52	
Core	−3.62	−1.27	−0.85	−0.74	−0.11	−0.06	
Main chamber	2.23	1.14	0.35	−4.47	−0.87	−0.63	
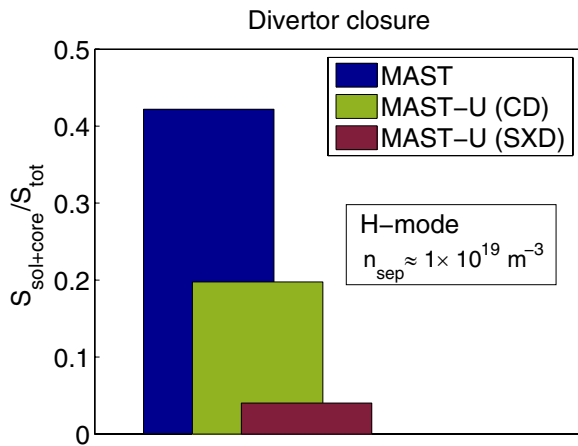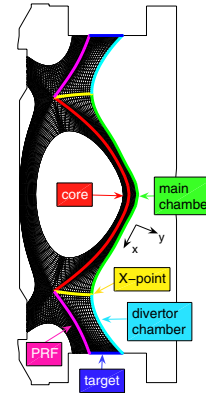
Figure 17. Divertor closure for case (a) measured as the ionization source outside the divertor with respect to the total ionization source for three different divertor configurations—MAST (figure in table 7), MAST-U with CD, MAST-U with SXD (figure 10).

comparable inside the simulation grid and they are larger at the midplane than at the X-point indicating that the molecules in the upstream SOL originate mainly from the main chamber (see also table 7 shown below).

An improved divertor closure in SXD is demonstrated in figure 17, where the divertor closure is measured as the ionization source outside the divertor with respect to the total ionization source. The comparison is shown for the H-mode plasma of $n_{sep} \approx 1 \times 10^{19} \, m^{-3}$, case (a), in three divertor configurations—MAST, MAST-U with CD and MAST-U with SXD, but the result is similar for cases (b), (c), (d). An improvement between MAST and MAST-U (a factor of 2) is caused by the baffle reducing the neutral and molecular fluxes from the divertor chamber to the main chamber. An additional improvement (a factor of 5) between CD and SXD is caused by larger collisionality in SXD (shorter mean free path and larger distance between the neutral source and the X-point) resulting in a reduced leakage of neutrals from the divertor to the upstream SOL.

In order to confirm that the ionization source in the upstream SOL originates from neutrals penetrating from the divertor, table 7 shows the fluxes of D_0 and D_2 in the simulation across the outer lower divertor and the upstream SOL. In spite of large D_0 flux from the target in SXD (one order of magnitude larger than in CD or MAST), the flux from the divertor to the upstream SOL across the X-point in SXD is by one order of magnitude smaller than in CD. Similarly, the molecular flux to the upstream SOL is reduced.

The molecular flux from the divertor to the upstream SOL is negligible in all configurations compared to the flux from the main chamber that is particularly large in MAST as there is no baffle, i.e. the divertor and main chambers are connected.

The atomic flux from the divertor region to the upstream SOL contributes largely to the flux to the core, as it is of the same magnitude. The flux to the core is clearly largest for MAST, both in terms of neutrals and molecules, and reduced in SXD (by a factor of 4 for D_0 and a factor of 12 for D_2 with respect to MAST). In MAST, the large atomic flux to the core results from the large escape of molecule flux from the divertor to the main chamber (no baffle) followed by dissociation in the upstream SOL.

Note that neutral–neutral collisions are not included in the EIRENE version used here. Nevertheless, we do not expect the neutral–neutral collisions to play a role in the studied MAST cases where the neutral densities at the target do not reach $\sim 10^{20} \, m^{-3}$ (figure 16).

3.4. Power losses and radiation

In the Super-X configuration, the plasma volume in the divertor is significantly increased. It is not obvious that this also implies a larger radiation volume and that longer $L_\parallel$ actually enables more power to be removed. On one hand, arguments for larger power losses in SXD are the better divertor closure resulting in higher neutral pressures and reduced temperatures at which radiation is effective. On the other hand, steeper parallel temperature gradients associated with longer $L_\parallel$ could shorten the region that radiates, as neutral/impurity radiation takes place only in a certain temperature band.

In order to compare SXD and CD in MAST-U, regions where the power loss exceeds a certain threshold are defined
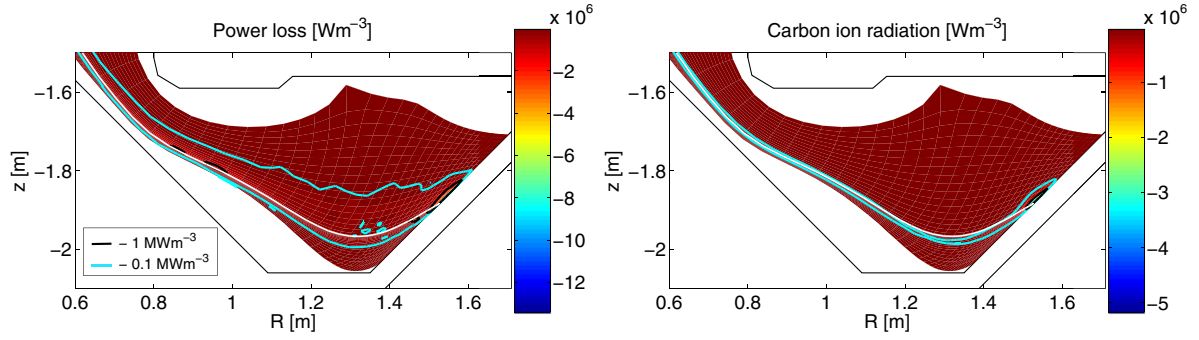
Figure 18. The SXD configuration—(left) distribution of total power losses for case (a). The contour lines show regions in the divertor where the power loss exceeds a certain limit. (Right) distribution of carbon line radiation. Compare with figure 7.
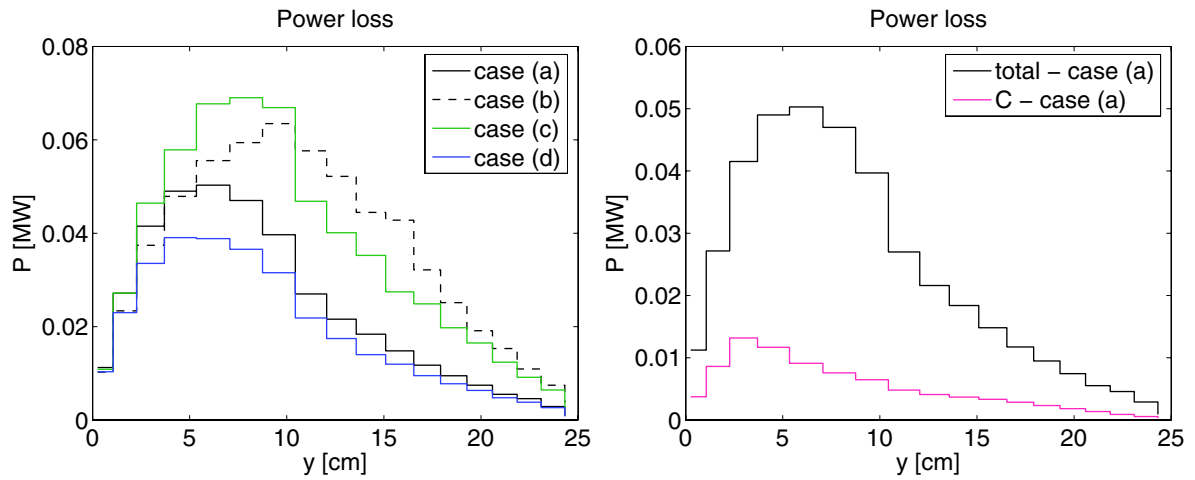
Figure 19. The SXD configuration—(left) volumetric power losses in the outer SOL calculated for each flux tube individually. All four cases are shown—the H-mode case (a) (solid), the L-mode case (b) (dashed), the higher density case (c) (green) and the lower power case (d) (blue). (Right) the total power loss and the loss due to carbon radiation are shown for case (a). Compare with figure 8.

and shown in figures 7 and 18 by contour lines. The black contour line (the power loss larger than 1 MW m^{-3}) shows that the most intensive loss is located very close to the target plate in a region with smaller temperatures and larger neutral densities. This region does not broaden in volume in SXD, however, it is small enough to neglect a substantial fraction of the power loss. The blue contour line in figure 18 on the left (the power loss larger than 0.1 MW m^{-3}) specifies a region where the power loss reaches 83% of the power loss in the divertor in SXD. The power loss rate is a magnitude smaller than in the black region, but it spreads over a much larger surface, and extends all the way from the target towards the X-point. In figure 18 right, only carbon ion line radiation is shown. The comparison with CD in figure 7 for the case (a) demonstrates that both the total power loss and carbon radiation regions stretch with $L_{\parallel}$ and the trend is similar for cases (b), (c), (d).

In figure 19, left, the radial distribution of the power losses is shown for all the studied cases. In figure 19, right, carbon radiation is separated for case (a), again indicating that deuterium dominates the power removal. As in CD, increased density or wider SOL support radiation losses through increased collisionality. In both cases (b) and (c), the power loss is larger both in terms of the amplitude and the radial extent. In the low power case (d), the radiation pattern

is similar to the one found in case (a), however more power with respect to P_{inp} is removed.

This is summarized in table 8 which also proves enhanced volumetric power losses in SXD in all cases compared to CD, as well as an expansion of the power loss area. The power loss caused by carbon ion radiation is separated and shows that the carbon radiation zone also expands in volume with increased $L_{\parallel}$ in SXD. In addition, the power radiated by carbon in the core is reduced in SXD with respect to CD (up to a factor of 0.6) at the same time as the power radiated in the SOL is increased (up to a factor of 2.3). Better impurity screening is achieved in SXD also in terms of carbon particle densities. Finally, the effect of carbon concentration has been tested by increasing the chemical sputtering yield from 1% to 3%. Stronger sputtering leads to 15–28% carbon radiation in the SOL, 2–3 times more than the lower sputtering yield. This also means that the ability of SXD to radiate more than CD is slightly larger for higher sputtering yields (see also section 3.5.4).

3.5. Particle and energy fluxes

3.5.1. Target fluxes. The energy flux at the target in SXD can be reduced with respect to CD by the effects of geometry (magnetic flux expansion), by volumetric power losses along

Table 8. The SXD configuration—the first four rows show the total volumetric power loss P_{vol} in terms of P_{inp} and the power loss due to carbon radiation separately in four SOLPS simulations (a), (b), (c) and (d) in different regions: (i) in the core (the closed field line part of the grid), (ii) in the SOL (the whole grid outside the separatrix), (iii) in the outer divertors (the region displayed in figure 7), (iv) in the blue region (defined in figure 7 by the contour line). The bottom rows show the surface S and the volume V of this region. The total power loss is calculated from EIRENE as the total energy loss caused to the plasma due to all plasma–neutral interactions including neutral and impurity radiation, charge exchange, ionization. Compare with table 3.

	Total				Carbon			
	(a)	(b)	(c)	(d)	(a)	(b)	(c)	(d)
P_{vol} in the core	4.7%	3.7%	1.8%	4.3%	0.8%	1.3%	1.0%	1.4%
P_{vol} in the SOL	28.9%	43.4%	41.1%	45.7%	8.1%	10.9%	9.6%	11.5%
P_{vol} in the outer divertors	25.5%	38.6%	37.5%	40.9%	6.1%	8.3%	7.3%	8.5%
P_{vol} in the blue region	21.2%	36.3%	34.3%	32.9%	3.3%	3.2%	3.8%	3.8%
S of the blue region [m^2]	0.158	0.275	0.230	0.137	0.026	0.037	0.030	0.026
V of the blue region [m^3]	1.170	2.026	1.649	1.015	0.186	0.260	0.217	0.189
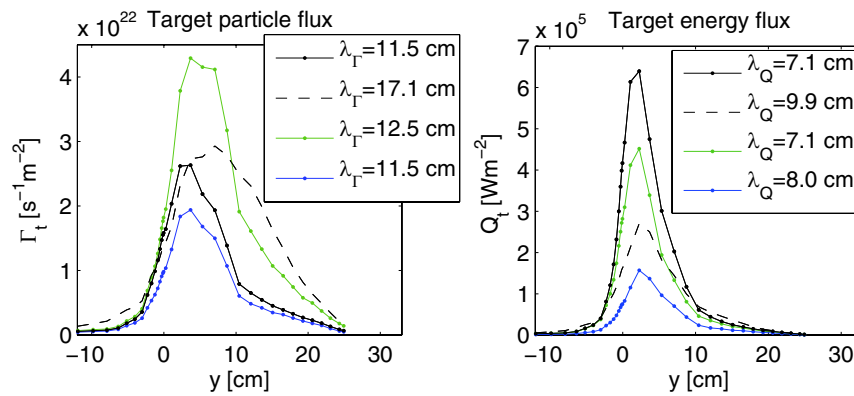
Figure 20. The SXD configuration—particle (deuterium ions) and power (deuterium ions plus electrons) loads at the outer target as functions of the target coordinate y for case (a) (solid), case (b) (dashed), case (c) (green) and case (d) (blue). Compare with figure 9.

the field line and by a broadening of the target wetted area due to radial transport. The magnetic flux expansion will be discussed in section 3.5.2 and the effect of radial transport in section 3.5.3.

Particle and energy fluxes deposited at the target in SXD are shown in figure 20. In the L-mode case (b), the target wetted area broadens and the peak Q_t drops with respect to the case (a). In the higher density case (c), Q_t drops at the same P_{inp} and λ_Q, as there is more power removed along the field line (this was not the case in CD in figure 9 where radiation had a smaller effect). In the case (d) where P_{inp} is a factor of 2 smaller, Q_t drops by a factor of 4 (more than in CD, again due to stronger power loss).

By changing the divertor geometry from CD to SXD, the peak Γ_t does not change (a larger flux expansion combined with stronger ionization source in the divertor), while the peak Q_t drops sharply (a larger flux expansion combined with larger volumetric power loss). This is demonstrated in figure 21 where a direct comparison between CD and SXD is presented for case (a).

The energy flux width in case (a) is $\lambda_Q^t \approx 7.1$ cm which corresponds to $\lambda_Q^u \approx 0.3$ cm (mapped to the midplane), and this is comparable to CD in section 2.5.1. The particle flux width $\lambda_\Gamma^t \approx 11.5$ cm mapped to the midplane as $\lambda_\Gamma^u \approx 0.5$ cm is also similar to the value found in CD. Cases (b), (c), (d), mapped to the midplane profiles have also the same widths, therefore the broadening of the energy flux at the target in

SXD with respect to CD is solely caused by the magnetic flux expansion (section 3.5.2), while the radial diffusion has no effect (section 3.5.3) in the simulations presented here. This effect will be investigated further in the near future for a broader range of input parameters.

Figure 21 at the top displays poloidal profiles of the particle and energy fluxes crossing the separatrix at the outer side. The input fluxes to the SOL between the X-points are the same in CD and SXD by prescribing the same n_{core} and P_{inp}. In addition, there is a non-negligible transport of the plasma from the main SOL below the X-point to the private flux region. The longer connection length in SXD allows more particles and energy to diffuse to the private flux region. The sharp negative peak at the target in SXD in the particle flux profile is due to the larger recycling source and target density in SXD.

In the middle row, the target particle and power loads are compared and the bottom row shows the same comparison in terms of the parallel fluxes. For the same flux into the SOL (top row), a factor 5.2 reduction of the power load Q_t is achieved at the target in SXD in case (a), and the peak parallel energy flux $Q_\parallel$ is reduced by a factor of 1.6. If we want to reduce the target power load to a similar level in the standard divertor, we would have to reduce the input power by this factor, unless we increase volumetric power losses in the SOL (e.g. by increasing the density to achieve more radiating regimes or detachment, or by radiating through injected impurities). The field line angle
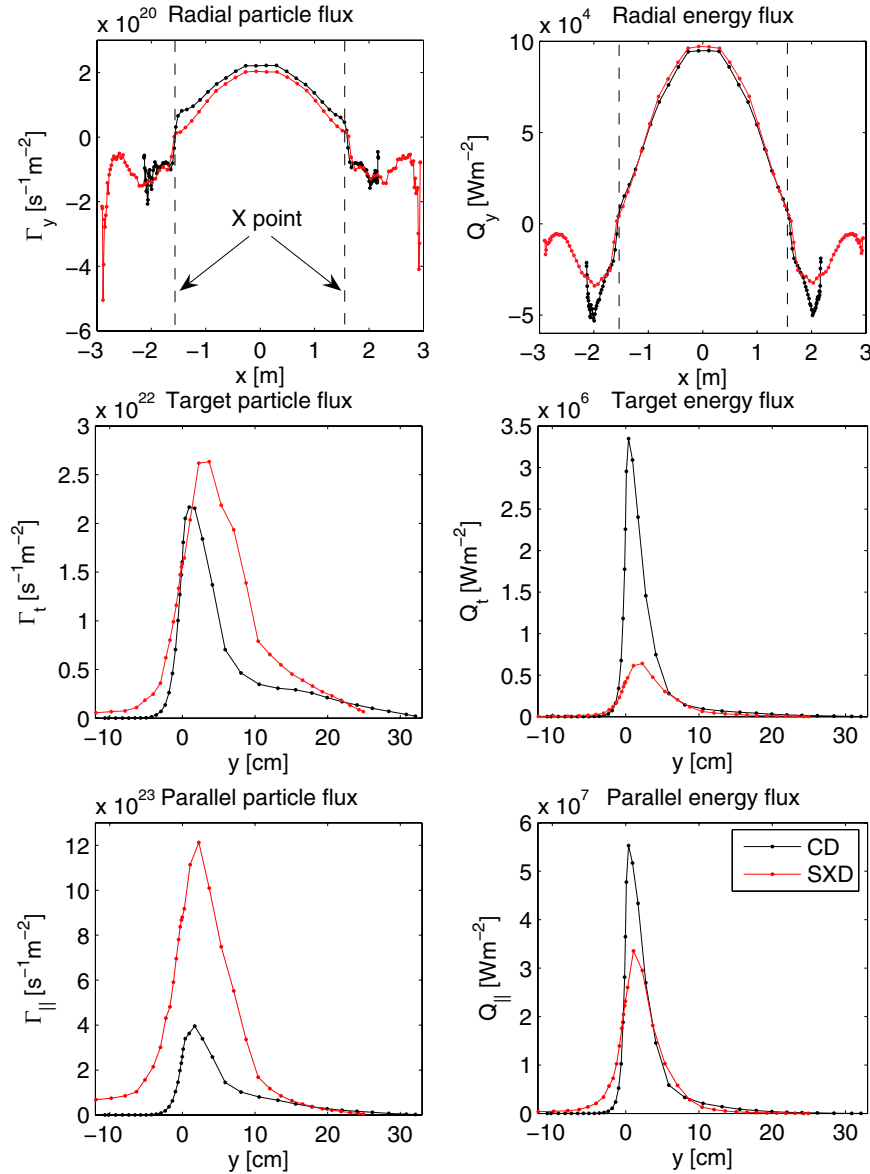
Figure 21. Direct comparison for CD and SXD in case (a)—(top) particle and energy fluxes crossing the separatrix at the outer side as functions of the poloidal coordinate x. (Middle) particle and power loads at the outer target as functions of the target coordinate y. (Bottom) parallel particle and energy fluxes at the outer target. The parallel fluxes are defined as: (i) the deuterium ion flux $\Gamma_\| = n_i u_\|$, (ii) the electron energy flux $Q_{\|,e} = 5/2 n_e u_\| kT_e - \kappa_e \partial(kT_e)/\partial s_\|$, (iii) the deuterium ion energy flux $Q_{\|,i} = 5/2 n_i u_\| kT_i + 1/2 m_i n_i u_\|^3 - \kappa_i \partial(kT_i)/\partial s_\|$.

at the target ϑ ($Q_t = Q_\| \sin\vartheta$) is $\vartheta \approx 3.5°$ at the separatrix in CD and drops to the critical value $\vartheta \approx 1°$ in SXD.

In the higher collisionality cases (b), (c), (d) with larger $\chi_\perp$, higher density or lower P_{inp}, the Q_t drop increases up to a factor of 9.1, see table 9 row (i), due to increased power losses. The effect of SXD on the reduction of Q_t also increases with the sputtering, see table 9 row (ii), as the power fraction radiated by carbon increases slightly more when the sputtering coefficient is increased in SXD than for the same increase in CD (tables 3 and 8). With stronger sputtering, carbon radiates more and the temperatures in the divertor are reduced. This also leads to the increased importance of other loss processes as well (e.g. charge–exchange). In cases (b) and (d) in row (ii) where the Q_t drop between CD and SXD is largest, the detachment threshold is reached in the SXD simulations.

Table 9. Reduction of the peak target energy flux in SXD with respect to CD in the simulations defined in table 1. The first row (i) is for the reference set of simulations with the chemical sputtering yield of 1%. The second row (ii) is for cases with increased sputtering yield of 3% to explore the effect of sputtering.

		(a)	(b)	(c)	(d)
Q_t drop	(i)	5.2	7.5	7.2	9.1
	(ii)	5.8	18.2	9.4	19.5

3.5.2. Flux expansion. One of the benefits of the SXD geometry is a large flux expansion in the divertor region resulting in a broadening of the energy deposition profile and a reduction of its peak value. For configurations in figure 10, the total flux expansion is responsible for approximately a factor of 4 reduction of the peak energy flux out of the total reduction shown in table 9.
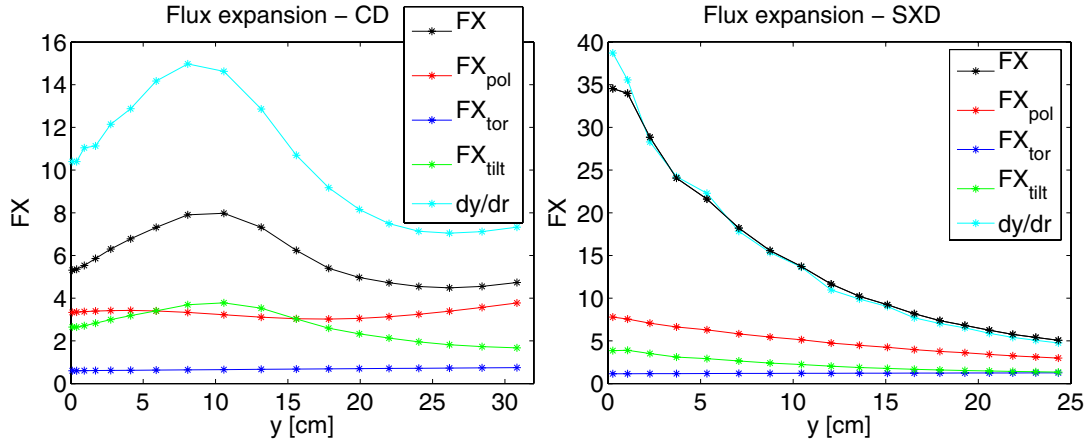
Figure 22. Flux expansion factors in CD and SXD as functions of the target coordinate y. The total magnetic flux expansion FX is separated into the poloidal flux expansion FX_{pol}, the toroidal flux expansion FX_{tor} and the expansion due to the target tilting FX_{tilt}. The expansion factor for mapping the target coordinate y to the radial midplane coordinate r is shown as dy/dr.

Table 10. The SXD configuration—flux expansion factors between the outer midplane and outer target. Compare with table 4.

	$\langle FX \rangle$	$\langle FX_{tor} \rangle$	$\langle FX_{pol} \rangle$	$\langle FX_{tilt} \rangle$	$\langle dy/dr \rangle$
Average over λ_Q	25.73	1.17	6.73	3.24	26.27
Average over λ_Γ	21.13	1.18	6.13	2.86	21.33

The flux expansion in CD and SXD at each radial position is shown in figure 22 for each expansion factor separately (see the appendix for a definition). In table 10, the effective flux expansion is shown as an average over 7 cm ($\approx \lambda_Q^t$), or alternatively over 11.5 cm ($\approx \lambda_\Gamma^t$). The values can be compared with table 4 for CD. The total effective flux expansion is a factor of 4.27 larger in SXD, mainly due to the toroidal flux expansion that accounts for a factor of 1.92 (the target at larger radius in SXD), and the poloidal flux expansion which is a factor of 1.98 larger (reduced poloidal magnetic field in SXD, see figure 10).

The reduction of the target energy flux in the H-mode case (a) in table 9 is not much larger than the reduction caused by the flux expansion, which can be interpreted in a way that it is mainly due to the magnetic topology that reduces Q_t, while radiation has a smaller effect. In cases (b), (c), (d) with larger collisionality, the volumetric power loss plays a more important role with respect to the flux expansion (table 9), i.e. one benefits from SXD more in high density or detached regimes with stronger radiation (discussed in [12]).

Two comments should be made regarding the reduction of Q_t in SXD. In case (a), the reduction by a factor of 5.2 seems to be a consequence of the flux expansion only (a factor of 4.27), in spite of a larger radiated fraction in SXD (see tables 3 and 8). One of the reasons is a displacement between the energy flux and radiation profiles (figures 19 and 20). Second, the power loss along the field line at the location of the peak Q_t is masked by stronger parallel heat transport in SXD and a consequent increase of $Q_\parallel$ in the near SOL driven by larger $\nabla_\parallel T$ in SXD. This has been analyzed in [9] and will be discussed also in the next section.

3.5.3. The role of $L_\parallel$ in SOL broadening. Another geometric feature of SXD is a long connection length in the divertor (figure 10). It is expected that longer $L_\parallel$ leads to a SOL broadening in the divertor as a consequence of the competition between parallel and radial transport (a longer distance to the target gives more time for spreading radially). However in the simulation, the SOL width in terms of λ_Q and λ_Γ is the same in CD and SXD when mapped to the midplane (sections 2.5.1 and 3.5.1) and there is also no obvious impact of the longer divertor on the radial locations of the peak target values of the density and temperature.

Let us therefore estimate the way $L_\parallel$ affects parallel losses. For particles, the parallel loss time can be defined as

$$\tau_\parallel^n \equiv \frac{n}{\nabla_\parallel (nu_\parallel)} \qquad (2)$$

using the continuity equation and assuming steady state. Equation (2) results in $\tau_\parallel^n = 0.68$ ms for CD and $\tau_\parallel^n = 1.7$ ms for SXD (calculated from values at the outboard midplane separatrix). Alternatively, $\tau_\parallel$ can be written as a function of $L_\parallel$ as $\tau_\parallel^n \approx L_\parallel/c_s$ if the approximation $\nabla_\parallel \approx 1/L_\parallel$ is used, leading to $\tau_\parallel^n \approx 0.16$ ms for CD and $\tau_\parallel^n \approx 0.32$ ms for SXD. In both cases, a longer time is needed in SXD for particles to reach the target (approximately a factor of 2), if we assume the same radial speed. The last assumption is justified by the usage of the same $D_\perp$ and fairly identical radial density profiles (figure 13).

For particles, however, it is not the transport from the upstream SOL and core that dominates, but the ionization source in the vicinity of the target (see figure 23, left). The Γ_t profile is correlated with the ionization source and the distribution of this source is a function of the atomic and plasma density, but also the plasma temperature. In addition to plasma–neutral interactions in the divertor, one can notice a non-negligible transport from the divertor region into the private flux region across the separatrix (figures 23 and 21 top), which can also contribute to the shape of the deposition profile.

For energy, the deposition profile is mainly determined by the power arriving from the upstream SOL and core (figure 23

16
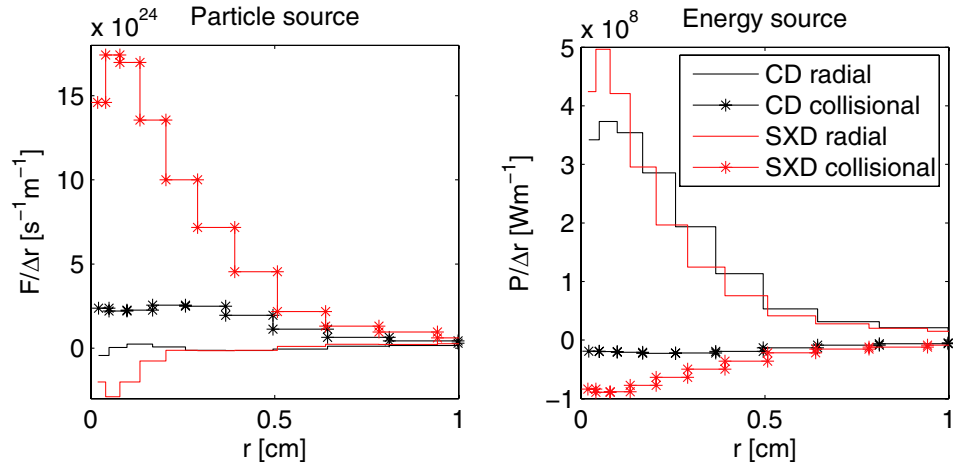
Figure 23. Magnitude of radial and collisional sources across the SOL. (Left) particle sources in each flux tube (displayed as the total integral source in the flux tube in [s^{-1}] divided by the flux tube width Δr) caused by radial transport and by recycling are shown for CD and SXD. For comparison, the profiles are mapped to the midplane coordinate r. (Right) energy sources separated radially and collisionally for each flux tube are shown. The gain of particles due to the radial transport is negligible in comparison to the ionization source in the divertor. In SXD, the radial source is negative in the near SOL, which means a particle sink from the flux tube to the private flux region). The energy transport is dominated by the radial fluxes, however, there is a larger energy loss in SXD due to cooling in the divertor.

Table 11. The SXD configuration—power and particle balance. Compare with table 5 where also all the quantities are defined.

	(a)	(b)	(c)	(d)
$P_{\text{sol,in}}$, $P_{\text{sol,out}}$	10.0%, 85.0%	11.8%, 83.9%	11.8%, 85.6%	11.1%, 84.5%
$P_{\text{t,in}}$, $P_{\text{t,out}}$	10.9%, 52.7%	11.8%, 31.6%	11.8%, 37.2%	10.9%, 29.9%
P_{wall}, P_{pfr}	1.5%, 1.6%	3.1%, 1.8%	2.5%, 1.7%	2.3%, 2.0%
P_{vol}	35.6%	53.7%	48.9%	56.9%
P_{vis}	2.4%	2.0%	2.1%	2.1%
F_{sol}	$3.7 \times 10^{21}\,\text{s}^{-1}$	$7.8 \times 10^{21}\,\text{s}^{-1}$	$7.2 \times 10^{21}\,\text{s}^{-1}$	$3.9 \times 10^{21}\,\text{s}^{-1}$
$F_{\text{sol,out}}$	81.1%	83.2%	82.5%	81.9%
$F_{\text{t,out}}$	$6.3 \times 10^{22}\,\text{s}^{-1}$	$10.0 \times 10^{22}\,\text{s}^{-1}$	$10.9 \times 10^{22}\,\text{s}^{-1}$	$4.5 \times 10^{22}\,\text{s}^{-1}$
$F_{\text{wall,out}}$	1.4%	1.9%	1.5%	1.7%

right). In the simulation, the transport process along the field line is a combination of convection and conduction, although conduction exceeds convection by 1–2 orders of magnitude, and electron and ion conductive losses are of comparable importance. A simple and often used approximation of the parallel loss time for energy $\tau_\parallel^E \approx 3nL_\parallel^2/2\kappa_e$ would result in $\tau_\parallel^E \approx 3.5\,\mu\text{s}$ for CD and $\tau_\parallel^E \approx 27.2\,\mu\text{s}$ for SXD and the longer $\tau_\parallel^E$ in SXD would indeed suggest a substantially wider SOL in terms of λ_Q. However, the SOLPS results show that unlike for the convection loss time, which can be approximated as $\tau_\parallel^n \propto \frac{L_\parallel}{c_s}$, the simple estimate above for $\tau_\parallel^E$ does not hold, as it appears we can not approximate the gradient length scale by $L_\parallel$ for the temperature. A more general form for $\tau_\parallel^E$ can be obtained using the energy equation and assuming steady state and conduction-dominated transport:

$$\tau_\parallel^E \equiv \frac{\frac{3}{2}n(T_e + T_i)}{-\kappa_e \nabla_\parallel^2 T_e - \kappa_i \nabla_\parallel^2 T_i}. \tag{3}$$

From equation (3), one obtains $\tau_\parallel^E \approx 3.8\,\mu\text{s}$ for CD and $\tau_\parallel^E \approx 2.7\,\mu\text{s}$ for SXD, i.e. comparable transport times in both geometries. In equation (3), the parallel gradient length for the temperature is shortened in SXD opposed to the simple approximation above where the gradient length grows with $L_\parallel$.

To conclude this section, the absence of an additional power and particle flux broadening in SXD in these simulations is explained by processes of the recycling (for particles) and the cooling (for energy), both affecting the parallel transport and playing a role in shaping the Γ_t and Q_t profiles. For energy, cooler plasma in the divertor in SXD leads to steeper parallel temperature gradients which drive stronger parallel losses cancelling the effect of longer $L_\parallel$. It is a different result to that expected and it is a consequence of different regimes in CD and SXD (SXD achieves cooling while CD does not). A detached regime where both CD and SXD divertor plasmas are cold should be investigated, as in such a case the difference in the parallel gradient length between CD and SXD is minimized. It is expected that the SXD advantages in such a case would be stronger.

3.5.4. Global balance. As for CD in table 5, global power and particle balance is calculated for the SXD simulations in table 11. Similar trends are found in SXD as in table 5—the volumetric power losses increase with larger radial transport and larger densities reducing the total power received by the targets. The particle and energy fluxes deposited at the outer wall are negligible compared to the target fluxes, even though little more power escapes into the private flux region as the

divertor leg gets longer. More importantly, compared with CD, the power deposited at the outer targets drops for the same power into the SOL by approximately a factor of 2 in cases (b), (c), (d) and 1.5 for case (a), and the particle load at the target is larger. In all cases, approximately twice as much power is removed from the plasma before reaching the target in SXD in comparison to CD, in these baseline simulations without any additional impurity species.

The volumetric power losses are caused by a combination of processes including impurity radiation, neutral radiation and all plasma–neutral energy exchange processes. The effect of carbon impurities is investigated separately. The power fraction radiated by carbon in SXD increases from 9–13% for the sputtering yield of 1% to 17–30% for the sputtering of 3%. For the case with a higher carbon concentration, the total power loss in SXD (42–73% of $P_{\rm inp}$) is again approximately double that in CD (19–34% of $P_{\rm inp}$), but the power to the outer targets is reduced more between CD and SXD than for lower carbon concentration (from $P_{\rm t,out} \approx$ 56–72% in CD to 14–46% in SXD). Therefore the effect of SXD on the reduction of $P_{\rm t,out}$ increases with increased carbon content.

4. Conclusions

The 2D SOL modelling code SOLPS has been used for a detailed comparison of example conventional and Super-X divertor plasmas in MAST. Although it is known that standard SOL transport codes encounter problems in the reproduction of high density experiments and have limitations in the physics they presently include, the codes are powerful for comparative studies where they can capture essential trends. The picture of the SOL transport is simplified in the sense that laminar transport is assumed on a constant-in-time magnetic equilibrium, radial transport is fixed and constrained typically as diffusive, kinetic and MHD effects are neglected, as is non-diffusive transport due to 3D turbulence (which would affect the value and nature of the SOL width). This approach limits the predictive capability of the codes (e.g. to determine the SOL width), but can be used to study parallel plasma transport from the core along the field lines to the divertor. The codes have special strength in coupling with the Monte Carlo description of neutral transport which allows to capture essential atomic physics playing an important role in the divertor modelling. Neutral–neutral collisions are not taken into account, but we do not expect them to have a significant effect in the studied cases as the input power and the neutral pressure in the divertor are not high enough.

Two divertor geometries—the conventional divertor (CD) and the Super-X divertor (SXD)—are confronted in the conditions of an inter-ELM H-mode MAST experiment with similar conditions in the core and upstream SOL. Four baseline simulations with different density, input power and radial transport are considered for each configuration, all with attached and non-seeded plasmas and a similar range of upstream parameters in CD and SXD (the temperatures of 62–114 eV in CD and 58–81 eV in SXD, the densities of $0.9–1.7 \times 10^{19}$ m^{-3}). As simulated by SOLPS, the SXD configuration of MAST-U proves to significantly reduce

the target energy fluxes even for attached hot plasma (a factor of 5.2–9.1 in our simulations compared to a factor of 4.3 caused by flux expansion). The target temperatures drop, allowing an earlier transition to the detachment (here by a factor of 3.2–7.1 from the sheath-limited SOL in CD with 44–108 eV to the high-recycling SOL with 7–27 eV in SXD). The effect of SXD on reducing the peak target energy flux is larger in regimes with higher density and wider SOL in which larger volumetric power losses are achieved. As a continuation, a comparison at high densities and detached regimes is presented in [12]. Note that drift effects have not been tested in the frame of this paper, however, they have been studied for MAST separately in [10]. The key role is played by the poloidal $E \times B$ drift, which in a connected double null configuration results in an asymmetry of the plasma parameters in the top and bottom divertors. In [10], the change in the electron temperature varies between 0–50% at the outer targets and this can for example affect the divertor detachment.

The divertor closure with respect to neutrals is increased in MAST Upgrade thanks to the separation of the upper SOL and divertor regions by a baffle and in SXD with respect to CD thanks to the shorter ionization mean free path of the recycled neutrals and longer distance between the neutral source and the X-point. The ratio between the ionization source outside the divertor and the total ionization source is reduced by a factor of 10 compared to the standard MAST divertor. As the result, the flux of neutral species to the core is reduced, here by a factor of 4 for deuterium atoms and a factor of 12 for molecules. The divertor in SXD is also more closed for impurities, as the power radiated by carbon in SXD is increased in the SOL, while it is reduced in the core.

In SXD with double the connection length, approximately double the power is removed from the plasma in the SOL volume before reaching the target by radiation and collisional processes (mainly charge exchange). The region from which the power loss occurs expands with increased $L_{\parallel}$ in the direction of magnetic field lines. The effect of SXD on reducing the power deposited at the target and the peak energy flux at the target also seems to increase with increased carbon sputtering yield.

For the same $D_{\perp}$ and $\chi_{\perp}$ in CD and SXD, the SOL width at the midplane is the same both in terms of n and T, while λ_Q and λ_{Γ} broaden at the target in SXD thanks to the magnetic topology. Opposed to expectations, λ_Q mapped to the midplane is comparable in CD and SXD and no obvious λ_Q broadening is found with increased $L_{\parallel}$ as the result of radial diffusion. The reason is the cooler plasma in the divertor in SXD in these cases and conduction-dominated parallel heat transport, thanks to which a steeper $\nabla_{\parallel}T$ in SXD leads to stronger parallel losses cancelling the effect of the longer parallel distance. If CD had a similar target temperature, the SXD advantages would be expected to be stronger. From the simulation, it also appears that the parallel loss time for energy cannot be approximated by the often used expression $\tau_{\parallel}^{E} \approx 3nL_{\parallel}^{2}/2\kappa_{\rm e}$ which misrepresents the dependence on $L_{\parallel}$.

In summary, this study has shown in detail where the SXD and CD differ and thus can guide future research to optimize the benefits of long-legged divertor configurations.

Acknowledgments

Appendix

Flux expansion in conventional and Super-X divertors

Flux expansion between the midplane and target, relating the target wetted area to the area in the upstream SOL,

$$ FX \equiv \frac{2\pi R^{\mathrm{u}}}{2\pi R^{\mathrm{t}}} \frac{\mathrm{d}y}{\mathrm{d}r} = \frac{R^{\mathrm{t}}}{R^{\mathrm{u}}} \frac{B_x^{\mathrm{u}} B^{\mathrm{t}}}{B^{\mathrm{u}} B_x^{\mathrm{t}}} \frac{1}{\sin\beta} \tag{4} $$

consists of the toroidal flux expansion FX_{tor} (related to the R coordinate, i.e. the toroidal magnetic field $B_z \approx B$), the poloidal flux expansion FX_{pol} (related to the poloidal magnetic field B_x) and the expansion due to the target plate tilting FX_{tilt},

$$ FX_{\mathrm{tor}} \equiv \frac{R^{\mathrm{t}}}{R^{\mathrm{u}}}, \quad FX_{\mathrm{pol}} \equiv \frac{B_x^{\mathrm{u}} B^{\mathrm{t}}}{B^{\mathrm{u}} B_x^{\mathrm{t}}}, \quad FX_{\mathrm{tilt}} \equiv \frac{1}{\sin\beta}. \tag{5} $$

Here, y is the target coordinate, r is the radial coordinate at the midplane, β is the angle between the field line and the target in the poloidal plane, B_x/B is the pitch angle. In the poloidal plane, the flux tube width expansion between the upstream and target locations can be expressed in terms of the poloidal flux expansion

$$ \frac{\mathrm{d}y}{\mathrm{d}r} = \frac{B_x^{\mathrm{u}} B^{\mathrm{t}}}{B^{\mathrm{u}} B_x^{\mathrm{t}}} \frac{1}{\sin\beta} \tag{6} $$

using the condition of the constant poloidal magnetic flux on a flux tube $h B_x/B = \mathrm{const}$ (h is the flux tube width and we assume $B \approx B_z \propto 1/R$).

The reduction of the energy flux between CD (index 1) and SXD (index 2) due to geometry effects can be estimated from a comparison of the target wetted areas. The parallel energy flux for the same input power changes due to the flux expansion as

$$ \frac{Q_{\|,1}}{Q_{\|,2}} = \frac{A_{\|,2}^{\mathrm{t}}}{A_{\|,1}^{\mathrm{t}}} \tag{7} $$

where $A_{\|}^{\mathrm{t}} = 2\pi R^{\mathrm{t}} \lambda^{\mathrm{t}} (B_x/B)^{\mathrm{t}}$ is the wetted area at the target normal to the parallel direction. Using $\lambda^{\mathrm{t}} (B_x/B)^{\mathrm{t}} = \lambda^{\mathrm{u}} (B_x/B)^{\mathrm{u}}$, the area can be expressed in upstream quantities. If we assume the same conditions in the upstream SOL for both configurations, the quantities expressed in the upstream location cancel and the final expression takes the form

$$ \frac{Q_{\|,1}}{Q_{\|,2}} \approx \frac{R_2^{\mathrm{t}}}{R_1^{\mathrm{t}}} \approx \frac{FX_{\mathrm{tor},2}}{FX_{\mathrm{tor},1}}, \tag{8} $$

i.e. the parallel energy flux in SXD is reduced by the effect of the magnetic topology due to the toroidal flux expansion. The reduced poloidal magnetic field in SXD accounts for the drop of the poloidal energy flux $Q_{\mathrm{pol}} = Q_{\|} B_x/B$ as

$$ \frac{Q_{\mathrm{pol},1}}{Q_{\mathrm{pol},2}} \approx \frac{R_2^{\mathrm{t}}}{R_1^{\mathrm{t}}} \frac{(\frac{B_x}{B})_1^{\mathrm{t}}}{(\frac{B_x}{B})_2^{\mathrm{t}}} \approx \frac{B_{x,1}^{\mathrm{t}}}{B_{x,2}^{\mathrm{t}}} \approx \frac{FX_{\mathrm{tor},2}}{FX_{\mathrm{tor},1}} \frac{FX_{\mathrm{pol},2}}{FX_{\mathrm{pol},1}} \tag{9} $$

and the target power load $Q_{\mathrm{t}} = Q_{\mathrm{pol}} \sin\beta$ is reduced as

$$ \frac{Q_{\mathrm{t},1}}{Q_{\mathrm{t},2}} \approx \frac{R_2^{\mathrm{t}}}{R_1^{\mathrm{t}}} \frac{(\frac{B_x}{B})_1^{\mathrm{t}}}{(\frac{B_x}{B})_2^{\mathrm{t}}} \frac{\sin\beta_1}{\sin\beta_2} \approx \frac{FX_{\mathrm{tor},2}}{FX_{\mathrm{tor},1}} \frac{FX_{\mathrm{pol},2}}{FX_{\mathrm{pol},1}} \frac{FX_{\mathrm{tilt},2}}{FX_{\mathrm{tilt},1}} = \frac{FX_2}{FX_1}, \tag{10} $$

involving also the expansion due to the target tilting.

References

[1] Ryutov D D *et al* 2008 *Phys. Plasmas* **15** 092501
[2] Valanju P M *et al* 2009 *Phys. Plasmas* **16** 056110
[3] Fishpool G *et al* 2013 *J. Nucl. Mater.* **438** S356
[4] Schneider R *et al* 2006 *Contrib. Plasma Phys.* **46** 3
[5] Shimada M *et al* 2007 Progress in the ITER Physics Basis *Nucl. Fusion* **47** S1
[6] Canik J private communications
[7] Lisgo S *et al* 2009 *ECA* **33E** O-4.046
[8] Havlíčková E *et al* 2013 *J. Nucl. Mater.* **438** S545
[9] Havlíčková E *et al* 2013 *Plasma Phys. Control. Fusion* **55** 065004
[10] Rozhansky V *et al* 2012 *Nucl. Fusion* **52** 103017
[11] Rozhansky V *et al* 2013 *Plasma Phys. Control. Fusion* **55** 035005
[12] Havlíčková E *et al* 2014 *Contrib. Plasma Phys.* **54** at press
[13] Rozhansky V *et al* 2009 *Nucl. Fusion* **49** 025007
[14] Wesson J 2004 *Tokamaks* (New York: Oxford University Press)
[15] Tskhakaya D *et al* 2008 *Contrib. Plasma Phys.* **48** 89
[16] Fundamenski W 2005 *Plasma Phys. Control. Fusion* **47** R163
[17] Elmore S *et al* 2013 *J. Nucl. Mater.* **438** S1212
[18] Petrie T W *et al* 2013 *J. Nucl. Mater.* **438** S166